AD

666 482

1.0	2.8	2.5
		2.2
1.1		2.0
		1.8
1.25	1.4	1.6

DISCLAIMER NOTICE

THIS DOCUMENT IS THE BEST
QUALITY AVAILABLE.

COPY FURNISHED CONTAINED
A SIGNIFICANT NUMBER OF
PAGES WHICH DO NOT
REPRODUCE LEGIBLY.

Department of Geology and Geophysics

Massachusetts Institute of Technology

Cambridge, Massachusetts   02139

RESEARCH IN SEISMOLOGY

Annual Report

To

Air Force Office of Scientific Research

1 November 1966 - 31 October 1967

ARPA Order No.   292 Amendment 29

Project Code No. 8652

Name of Contractor - M.I.T.

Date of Contract - November 1, 1965

Amount of Contract - $514,598.00

Contract No. AF 49(638)-1632

Contract Termination Date - October 31, 1968

Project Scientists - Frank Press, 617-864-6900, ext. 3382
                     M. Nafi Toksöz, 617-864-6900, ext. 6382

Short Title of Work - Research in Seismology

ABSTRACT

The seismic research activities carried under the contract AF 49(638)-1632 are grouped in four categories.

In the first, the utilization of LASA data for various seismological studies is discussed. P-wave velocity-depth distribution in the mantle is obtained along two profiles. Frequency-wavenumber structure of microseisms are investigated using both the long and short period data from LASA, and it is found that at periods shorter than 5 seconds predominant noise peaks correspond to higher mode Rayleigh waves and P-wave noise.

The structure and inhomogeneities of the upper mantle are studied using seismic and other geophysical data. In Japan the surface wave dispersion data are best fitted by a model containing thin soft layers in the upper mantle. Seismic, heat flow, geopotential, surface topography and crustal data are correlated using coefficients of spherical harmonics up to the third order. It is found that some lateral density variations may exist in the upper and lower mantle.

The near source and far-field seismic data from the Parkfield earthquake of 1966 are analyzed for source mechanism and attenuation studies. The stress drop associated with this earthquake is estimated to be about twenty bars. Some peaks and regional differences are found in attenuation curves for the Rayleigh and Love waves.

CONTENTS

I. INTRODUCTION

The research efforts under this contract have been directed
primarily to the study of earth's crust and mantle and to the
investigations of the earthquake source mechanisms. Seismic
data from the Large Aperture Seismic Array as well as single
stations have been utilized in these investigations. In this
report, different studies are grouped in four chapters on the
basis of type of data use and the problems studied.

Large Aperture Seismic Array has been one of the main data
source. Using LASA data we have investigated the velocity
distribution in the mantle and the mode structure of micro-
seisms. To determine the variations in the crustal structure
under LASA we have initiated a surface wave dispersion program
for structure determinations.

Data from other stations and other sources have been
utilized to determine the structure and inhomogeneities of the
upper mantle. These include surface wave studies in selected
areas, global distribution of seismic residuals, geopotential and
heat flow variations, and crustal properties.

The source mechanism studies have been pursued theoretically
and in conjunction with Parkfield earthquake.

In addition to above topics a brief description of a
LASA tape library and a new vibrator type seismic energy source
are given in this report.

II. UTILIZATION OF LASA FOR THE STUDY OF SEISMIC PHENOMENA AND THE EARTH'S DEEP INTERIOR

II. 1   Lateral Variations in Mantle P-wave Velocities Determined From $dT/d\Delta$ Measurements at LASA

The fundamental relationship in earthquake seismology is the one between the travel-time of seismic waves from source to receiver and the seismic velocity distribution within the earth. If the seismic wave travel-time is known for all epicentral distances so that its derivative, i.e., $dT/d\Delta$ is known, then it is a relatively simple matter to derive the seismic velocities within the earth to the depth at which the deepest rays penetrate (Bullen, 1960). Travel-time curves as a function of epicentral distance, based on the observations of many thousands of earthquakes, are available; and traditionally the quantity $dT/d\Delta$ has been determined by smoothing and differentiating these curves. However, this method has drawbacks since errors in the travel-times are amplified, and smoothing of data will prevent the detection of azimuthal asymmetries in the earth's velocity structure.

Therefore we have been using data from LASA to measure $dT/d\Delta$ directly for each event. There are several advantages to this; the principal one is that we avoid using absolute travel-times which are subject to error due to error in the source location. Another advantage is that no smoothing of

data is necessary: the wavefront slope is determined uniquely for each earthquake and can therefore be analyzed in the light of its particular source location and travel path.

Results thus far have been good. If all 21 subarrays are used in the analysis, the precision in measuring $dT/d\Delta$ (assuming an unbiased reading error of $\pm$ 0.05 seconds) is within 0.03 seconds per degree. This is certainly better than anything we could get from differentiating total travel-time curves, which are only accurate to about 0.1 seconds.

Unfortunately there are some difficulties. The earth's seismicity does not provide earthquakes over all range of epicentral distances and azimuths from LASA. There is, for example, a notable lack of information for epicentral distances less than about 25 degrees. However the earthquake density at epicenter distances between 25 and 90 degrees is high and fairly well distributed along two azimuthal directions. The directions are from 295° to 315° and from 135° to 160° measured from LASA. In order to minimize uncertain crustal and subcrustal effects on the wavefront and to look for possible lateral inhomogeneities in the lower mantle, we shall analyze these two azimuthal directions separately.

A more serious difficulty is the effect that the velocity structure in the crust and upper mantle below LASA have in distorting the wavefront. We are interested in obtaining the mantle velocities and therefore must remove, or at least understand, this distortion. At this point we do not know the geologic structure below LASA well enough to apply station

-4-

corrections that will compensate for the crustal distortion.
Therefore we limit our interpretation to those parts of the
dT/d A- vs - A curves which are not ambiguously affected by
the crust and upper mantle inhomogeneities. The effect on the
wavefront due to these inhomogeneities is observed to be a
function of both azimuth and epicentral distance to the source,
although it is more strongly a function of azimuth. Since we
analyze events to the northwest of LASA separately from those
to the southeast, we are comparing ray paths which sample
approximately the same crust and upper mantle at LASA and are,
to a first approximation, affected in the same way. We can
measure what this effect is by comparing observed total
travel times with travel times obtained by integrating under
the dT/dA - vs - A curves (Chinnery and Toksöz, 1966). These
times must, to the degree of accuracy in our measurements, agree.

II. 2   Measurements of dT/dA

We have measured dT/dA for approximately 400 earthquakes
of which 137 lie within the azimuth interval of 295° to 315°,
and 74 lie within the interval of 135° to 160°. They are denoted
by separate symbols and plotted as a function of epicentral
distance on Figure 1. The epicentral distances were obtained
from E.S.S.A.'s "Preliminary Determination of Epicenter" cards
and have been corrected for depth of focus by a straight-line

extrapolation from the earthquake hypocenter to the surface. The data have not been corrected for hypothesized crustal or upper mantle structure below LASA, but the several small changes in slope, which are seen on both $dT/d\Delta$ - vs - Δ curves, are defined by rays which traverse almost the same path in the LASA crust and subcrust. Therefore it seems more reasonable to believe that such changes in slope are caused by changes in the velocity gradient in the lower mantle near the ray vertex-- or, at the source.

The method of determining $dT/d\Delta$ was to measure the relative arrival times of a seismic wave at each LASA subarray and calculate, by the method of least squares, its horizontal phase velocity. The value of $dT/d\Delta$ is equal to the horizontal phase velocity divided into the radius of the earth (see, for example, Bullen, 1963). The relative arrival times were measured by the staff of the Seismic Data Laboratory of Teledyne Industries and are available in their report No. 172. From both the results of our calculations and personal communication with the staff of S.D.L., we feel that the arrival times are accurate to about $\pm$ 0.05 seconds. However in most cases not all 21 subarrays were used in recording the arrival times; which, because of the anomalous structure below LASA, introduces a bias in the calculation. This, coupled with possible errors in the epicentral distances, probably accounts for most of the scatter in the curves of Figure 1.

The difference in the two curves is striking. We feel
that the large separation between them is due to near-surface
lateral inhomogeneities below LASA. However, the small changes
in slope, which appear in several places along both curves
(for example: at 35 degrees), may represent velocity gradients
in the lower mantle which are different along the northwest
and southeast azimuths.

A correction term for the northwest-azimuth curve has
been determined by Chinnery and Toksöz (1966) to be +0.05
seconds per degree. This was based on making the total travel
time, as a function of distance, which was obtained by integrating
the $dT/d\Delta$ - vs - Δ curve, agree with the total travel time as
observed for a well documented nuclear explosion (Longshot). As
a first-order correction to the southeast-azimuth curve, we
have subtracted 0.44 seconds per degree. The most compelling
reason was that this curve now coincides with the corrected
northwest-azimuth curve at the value of delta where our data
begin, i.e. 30 degrees.

The correction for the southeast-azimuth curve is partly
substantiated when we compare the total travel times for some
southeast events with the total travel times expected from
the integration of the southeast $dT/d\Delta$ - vs - Δ curve. Since

there is no data for events less than 30° from LASA, we have assumed that, at 30°, the integrated total travel time is the same as the average of the observed travel times. Figure 2 shows the observed and integrated total travel times, after subtracting the J B values, plotted as a function of epicentral distance. The various curves are the integrated times after shifting the dT/dΔ - vs - Δ curve as noted. It appears that a correction to the dT/dΔ - vs - Δ curve of -0.44 seconds per degree is needed to bring the integrated travel times at least into partial agreement with the observations.

The agreement, however, is only fair; it is particularly bad around 5500 kilometers. The origin times of the observed events are based on the "Preliminary Determination of Epicenter" cards and are accurate to within several tenths of a second. Most of the scatter in Figure 2 is probably due to errors in reading the absolute arrival time and lack of information on focal depth. Because of this "only fair" fit and for other reasons that will be discussed below, we feel that other station corrections are necessary for the southeast-azimuth eve .

We were tempted to draw the line on the southeast-azimuth dT/dΔ curve through the four points at about 67 degrees. They would define, then, a very sharp change in the slope which could be interpreted as an anomalous change in the velocity gradient in the lower mantle. However, we have assumed they are

part of the scatter and drawn a smooth curve past them. There are two reasons: number one is that a change in slope does not appear on the northwest-azimuth curve, and number two, it would aggravate the discrepancy between integrated and observed total travel time as seen on Figure 2.

III.   Mantle Velocity Distribution Based on Measurements of $dT/d\Delta$

The velocity distribution within the earth which agrees with the corrected $dT/d\Delta$ -- vs - Δ curves is shown on Figure 3. Since we have no data at distances closer than 30° from LASA, we must assume some velocity model for the upper mantle. We have adopted that used by Chinnery and Toksöz (1966), although it should be noted that the upper mantle structure has small effect on the parameters of a ray whose vertex is in the lower mantle. Figure 4 illustrates this; here we show the $dT/d\Delta$ - vs - Δ curves for a velocity model which best fits the observed data for the northwest-azimuth events. One curve, however, has upper mantle velocities (to a depth of 650 kilometers) according to model CIT 11, which is presumed to be a typical upper mantle velocity structure for oceanic regions (Anderson, 1965). The other has the upper mantle velocities used by Chinnery and Toksöz, which has been assumed for typical tectonic regions. The two curves are almost identical for epicentral distances greater than 30 degrees. At 30 degrees the ray bottoms at a depth of about 750 kilometers---only 100 kilometers below the lower boundary of the two models.

The method of obtaining the velocity structures along the
two azimuths was essentially one of direct trial and error
as used by Chinnery and Toksöz (1966). A spherically symmetric,
layered earth is assumed and a velocity at each layer boundary
is assigned. The velocity could be specified to be constant
in each layer or else to have the form $V = V_o r^?$
where V is the velocity at a distance r from the center of
the earth (Bullen, 1960). In the calculations we use $dT/d\Delta$,
which for a given ray is constant through its entire travel
path, as the independent variable. The total travel time,
distance, and depth of ray vertex is calculated for all
$dT/d\Delta$'s. The earth model is continually altered until the
calculated distances match the observed epicentral distances
for all $dT/d\Delta$'s. For a given $dT/d\Delta$, changes in the calculated
epicentral distance are so sensitive to changes in the velocity
gradient at the ray vertex that the precision in determining
the relative velocities in the lower mantle is within 0.02
km/sec. There are, however, distance intervals where no
$dT/d\Delta$ information is available; and as a result, there are
depths in which we had to assume or interpolate the mantle
velocity. (For example, the entire upper mantle above 650
Kilometers.) These areas are denoted by solid lines in the
velocity-vs-depth curves of Figure 3.

We intrepret the small changes in the slope of $dT/d\Delta$ vs Δ to be caused by a change in the velocity gradient near the depth at which those rays bottom. Thus the sharp increase in the slope of $dT/d\Delta$ at about 35 degrees corresponds to a decrease, then increase, in the velocity gradient between the depths of 775 and 850 kilometers. This is seen along both the northwest and southeast azimuths and therefore suggests that it may be a widespread, significant feature of the mantle. It is very doubtful that local inhomogeneities below either the source area or LASA would cause these similar discontinuities since the rays defining them traverse different paths. The only thing in common for these ray-paths is their approximate vertex depth, which is the most sensitive area in determining the total travel path of the ray.

It does appear, however, that the change in slope along the northwest azimuth is somewhat sharper and occurs at a slightly greater epicentral distance--thus the separation in the velocity-vs-depth curves at about 800 kilometers. Because of the scatter and the lack of data, particularly from the northwest, we cannot tell if this separation is significant.

At greater distances, and hence greater vertex depths, there do not appear to be any other discontinuities common to both $dT/d\Delta$ - vs - Δ curves. For northwest azimuths we see the changes in slope at about 55 degrees and 70 degrees which have been discussed in detail by Chinnery and Toksöz (1966). These have been interpreted to be caused by decreases in the velocity gradient at depths of about 1300 and 2000 kilometers respectively.

At about 87 degrees the slope of the northwest curve decreases sharply, and the scatter of points increases. This effect has also been noted by Lane Johnson (1966) at the Tonto Forest Seismological Observatory (TFSO) in Arizona. He has interpreted this as a triplication in the $dT/d\Delta$ - vs - Δ curve resulting from a zone of almost constant velocity between the depths of 2670 and 2800 kilometers.

Because the data of Lane Johnson is an independent measurement of $dT/d\Delta$, taken at another location, it is interesting to compare his results with ours. On Figure 5 we have reproduced his curve of horizontal phase velocity . (which is proportional to the inverse of $dT/d\Delta$) and compared it to the LASA curves for both azimuths. Here we have already applied the corrections of +0.05 and -0.44 sec/deg to the $dT/d\Delta$ values for the northwest and southeast azimuth events respectively. Johnson felt that he could remove the effect of crust and upper mantle inhomogeneities with station corrections applied to the raw data, and he therefore did not separate the data according to source.

The general features of the three curves are somewhat different; and until more information is available, we can only speculate that these differences are due to distortion of the wavefronts in the crust and upper mantle below LASA. To some extent also, the TSFO data may still be biased by near-surface structure.

There are however two features on these curves to which we attach some significance. One is the increase in slope between 35 and 40 degrees which appears on all three curves and which has been interpreted as a change in the velocity gradient between the depths of 775 and 850 kilometers. The other is the sharp decrease in slope for both the LASA-northwest and the TFSO curves beginning at about 89 degrees. As with TFSO, there could very well be triplication on the LASA curve. Since it appears on both curves, we feel it is significant and interprete it to be caused by a decrease in the velocity gradient beginning at about 2500 kilometers--possibly due to the influence of the core.

The southeast-azimuth curve does not show the change in slope at 70 degrees as does that of the northwest. The data are numerous here and this discontinuity is clearly absent. Actually the slope of the two curves is quite different beyond 60 degrees, and this accounts for the separation in the velocity-depth functions below about 1600 kilometers. Below this level the velocity-depth relation derived from the southeast data is much smoother--almost identical to that derived from Jeffreys-Bullen times. The southeast data stops at about 87 degrees so we cannot verify the change of slope which occurs on the other curve at this distance.

There is not enough data from the southeast azimuth
to determine the presence or absence of the 55° discontinuity
which has been observed for the northwest-azimuth events.
(Chinnery and Toksöz, 1966)

IV. · Time Residuals and Relative Amplitudes

Measuring the horizontal phase velocity of a seismic
wavefront propagating across LASA is equivalent to finding
the best fitting plane to the wavefront. In an attempt to more
accurately understand the wavefronts, we have also fit them,
by the method of least squares, to a quadratic surface. We
have used the time residuals to estimate the quality of fit.
Time residuals for a given subarray are determined by subtracting
the relative arrival time expected by the calculated plane or
quadratic wavefront from the observed relative arrival time.

It has been observed that, for a given epicenter, the
residuals can be predicted to an accuracy of about 0.05
seconds. In order to study these residuals as a function of
epicenter, we have taken intervals along the northwest and the
southeast azimuth where a large number of earthquakes in our
study had occurred. Table 1 shows these regions and their
location relative to LASA. We then determined the average
time residual at each subarray for the events within each
sector. The standard deviation of these averages was almost
always less than 0.05 seconds.

Table I

Epicentral regions involved in the study of plane and quadratic wave time residuals

	Area	Azimuth	Distance	No. of Events
1.	So. Alaska and Kodiak	307-314	3300-3400	11
2.	Near Is., Rat Is.	305-308	5400-5660	16
3.	Kamchatka	312-314	6600-7000	11
4.	Kuriles-Hokkaido	311	7400-7800	13
5.	Honshu	308-310	8400-8800	11
6.	So. Mexico	152-160	3600-4000	8
7.	No. Columbia	134	5400-5500	10
8.	Peru	142-148	7400-7800	9
9.	No. Chile, Argentina	145-146	8400-8800	10

It is clear that lateral crust and upper mantle inhomo-
geneities are perturbing the wavefront, and we can tentatively
identify which subarrays are causing the most trouble. Using
both relative time residuals with respect to the best fitting
plane wave and relative amplitudes at each subarray we can
outline areas of relatively high and low velocities below
LASA. They are so located that wavefronts from the southeast
are more highly perturbed than those from the northwest .
We have not yet applied station corrections to account for these
anomalous zones, but we have tried to limit our interpretation
to these parts of the $dT/d\Delta$-vs-Δ curve that are not ambiguously
affected by them.

It is very curious that the wavefronts of events coming
from the northwest of LASA are so much different than those
o. the southeast. Apparently there is some velocity inhomogeneity
in the crust or upper mantle southeast of the array center so that
rays coming from the northwest are not affected by it. Roy
Greenfield (personal communication) of Lincoln Laboratory has
shown that these time anomalies could be explained by about
a 30 kilometer segment of the Moho which dips 18 degrees to the
northwest. This segment would be centered about 15 kilometers
southeast of the array center. While such large structures
appear to be necessary to explain the time anomalies, they are
supported by neither seismic refraction nor gravity data
(Steinhart, et al, 1961; Borcherdt and Roller, 1967). This is
one of the major problems confronting us at present.

We have compared the plane wave time residuals with the
relative amplitudes observed at LASA. For most of the regions
in which we have analyzed the time residuals, we also have data
on the relative amplitudes (Seismic Data Laboratory report
No. LL-4). Table 2 shows the epicenter regions and the number
of events studied in each region; Table 3 shows the average
relative amplitude and its standard deviation as seen by each
subarray for each epicentral region. The relative amplitudes
were normalized with respect to the geometric mean for each
event; that is, the relative amplitude at station j due to,

earthquake i is

$$Y_{i,j} = L_{i,j} \Big/ \left\{ \prod_{j=1}^{N} L_{i,j} \right\}^{1/N}$$

where L is the observed amplitude (corrected for variations in instrument gain) and N is the number of subarrays observing that particular earthquake. When we use the term relative amplitude, we are referring to the normalized value Y.

The number of events per sector listed in Table II is sometimes less at certain subarrays due to poor signal quality or inoperation. Whenever this number is less than 3 or whenever the listed amplitude is inconsistent with that of adjacent epicentral regions, the relative amplitude for that sector is omitted.

Figures 10 and 11 are the plane wave time residuals for the northwest and southeast azimuths plotted against the relative amplitudes. Positive time residuals, as defined here, are late arrivals relative to the best fitting plane wave, and the actual wavefront shape may be concave upward at this point. Ideally the concave upward wavefront also represents a focusing of energy so that the relative amplitude will be greater. Conversely, negative residuals could mean a concave downward wavefront and thus have lower amplitudes.

That such a relationship exists is well illustrated by Figures 10 and 11. There are some exceptions however, but these may be due to the attitude of the calculated plane rather than a higher-order distortion of the wavefront. As a matter of fact, we may have here a clue as to which residuals are due to the crust and upper mantle effects on the wavefront and which are due to biasing of the calculated plane created by anomalous time delays at other subarrays.

IV. 1 Anomalous Velocity Zones Below LASA

Table LV lists the subarrays, plane wave time residuals, relative amplitudes, and epicentral regions for which the relative amplitudes exceed (or are less than) unity by an amount greater than the standard deviation. This is true for about half the total number of subarrays, and in over 80% of the cases, the plane wave time residuals are consistent with the relative amplitude; that is, the plane wave time residuals are positive for high relative amplitudes and negative for low. The correlation is particularly striking for the southeast azimuths where the agreement reaches 94%.

For events from the southeast, we see that the southern subarrays (F3, F2, and F3; see Fig. 12) have positive residuals and high amplitudes relative to the rest of the array. However, if anomalously low velocity layers underlie thes. subarrays, the measured dT/dΔ values for southeast events would be lower, instead of higher, than those of northwest events. Therefore, in order to make the bias in the wavefront consistent with the plane wave residuals and relative amplitudes, subarrays F2, D1, D2, C1, C2, B1, and B2 must be anomalously fast. For these same reasons, subarrays D4, E1, and E4 appear to be slow--again for events from the southeast.

The plane wave time residuals and relative amplitudes for the northwest events are consistent with those for the southeast. The anomalously slow .rustal or subcrustal velocities seen by the southeast-azimuth rays at ' 'arrays D4, E1, and E4 is approximately the same as that seen by the northwest azimuth rays going to the subarrays of the B and C ring. These, for the most part, also show positive plane wave residuals and high relative amplitudes. Since the inner subarrays have less affect on the plane wave determination, we do not see a large offset on the dT/dΔ values calculated for the events from the northwest. Furthermore the crustal and subcrustal structure traversed by the anomalously fast rays, coming from the southeast and seen at subarrays E2, D1, D2, etc., may not be observed for northwest raypaths; that is, there are no

subarrays at the point of emergence of these rays.

This pattern of anomalous velocities is consistent with the offset of the two $dT/d\Delta$-vs-Δ curves of Figure 1. However, in order to create a change in the calculated $dT/d\Delta$ of 0.5 seconds per degree, approximately 2 seconds of total delay time must be distributed among the perturbed subarrays. Furthermore, this delay must be heavily weighted on the outside subarrays.

The next step of course, would be to interprete these velocity anomalies and apply the necessary station corrections to offset them. At this point however, we feel that better resolution in these crustal or upper mantle inhomogeneities is necessary in order to prevent biasing the data with poor station corrections.

V. Summary and Conclusions

We have used relative arrival times at LASA to measure $dT/d\Delta$ as a function of Δ. The data has been separated into azimuth intervals 295°-320° and 135°-160° for which, beyond a distance of 30°, there is a fairly good distribution of earthquakes.

The resulting curves of $dT/d\Delta$-vs-Δ for the two azimuths are quite different. There is an offset of approximately 0.5 sec/deg which we have interpreted to be caused by lateral inhomogeneities in the crust and upper mantle below LASA. On the basis of the work by Chinnery and Toksöz and on some of our own measurements of total travel time, we have applied a correction of -0.44 sec/deg to the southeast-azimuth curve and +0.05 sec/deg to the northwest azimuth curve.

Both curves of $dT/d\Delta$-vs-Δ show a relatively large change in slope at about 37 degrees which corresponds to a decrease, then increase, in the velocity gradient beginning at the depth of about 775 kilometers. It appears that such a change in gradient is a widespread and major feature of the mantle.

Other small second order discontinuities, which appear on the northwest-azimuth curve, are either absent on the other curve or are located at distances where southeast data are missing. The most notable difference in the two curves is between 65 and 75 degrees, where the density of points is high for both curves. For the northwest azimuths the slope is less, and there is a slight kink in this curve at about 70 degrees. Our interpretation is that the velocity gradients in the lower mantle are slightly different along the two azimuths. Beginning at about 2500 kilometers, both LASA and TFSO detect the beginning of a decrease in the velocity gradient with the possibility of a thick zone of constant, or low, velocity above the core mantle boundary.

It is clear that lateral crust and upper mantle inhomo-
geneities are perturbing the wavefront, and we can tentatively
identify which subarrays are causing the most trouble. Using
both relative time residuals with respect to the best fitting
plane wave and relative amplitudes at each subarray we can
outline areas of relatively high and low velocities below
LASA. They are so located that wavefronts from the southeast
are more highly perturbed than those from the northwest .
We have not yet applied station corrections to account for these
anomalous zones, but we have tried to limit our interpretation
to these parts of the $dT/d\Delta$-vs-Δ curve that are not ambiguously
affected by them.

REFERENCES

1. Anderson, D.L., 1965. Recent evi nce concerning the structure and composition of the earth's mantle, Physics and Chemistry of the Earth, 6, 1-129.

2. Borcherdt, C.A., and Roller, J.C., 1967. Preliminary Interpretation of a Seismic-Refraction Profile Across the Large Aperture Seismic Array, Montana, Tech. Letter 2, National Center for Earthquake Research.

3. Bullen, K.E., 1960. A new method of deriving seismic velocity distributions from travel-time data, Geophys. J., 3, 258-269.

4. Bullen, K.E., 1963. An Introduction to the Theory of Seismology, Cambridge University Press.

5. Chinnery, M.A., and Toksöz, M.N., 1967. P-wave velocities in the mantle: I, below 700 Km., Bull. Seism. Soc. Am. 57, 199-227.

6. Johnson, L., 1966. Measurements of Mantle Velocities of P-Waves With a Large Array, Ph.D. Thesis, California Institute of Technology.

7. Seismic Data Laboratory, Teledyne Inc., 1966. LASA Travel-Time Data at the SDL, Report No. 172, 5 December, 1966.

8. Seismic Data Laboratory, Teledyne Inc., 1967. Amplitude Anomalies at LASA, Report No. LL-4, 9 January, 1967.

9. Steinhart, J.S., and Meyer, R.P., 1961. Explosion Studies of Continental Structure, Carnegie Inst., Washington Publ. 622.

Table II

Epicentral regions involved in the study of relative amplitudes

	Area	Azimuth	Distance	No. of Events
1.	Near Is., Rat Is.	305-308	5400-5660	8 - 10
2.	Kuriles, Hokkaido	311	7400-7750	6
3.	Honshu	308-310	8400-8750	6
4.	No. Columbia	134	5400-5500	6
5.	Peru	142-148	7400-7750	6
6.	No. Chile, Argentina	145-146	8400-8750	7

Table III

SUBARRAY	AREA I		AREA II		AREA III		AREA IV		AREA V	
	AMP	ST DEV	AMP	ST DEV	AMP	ST DEV	AMP	ST DEV	AMP	ST DEV
A0	.88	.08	.82	.16	1.08	.14	.41	.22	.66	.14
B1	1.35	.06	.63	.08	.77	.12	.53	.10	.57	.06
B2	1.56	.09	1.52	.10	1.51	.05			.74	.13
B3	.71	.15	1.26	.09	1.38	.11	.85	.06	.95	.10
B4	1.01	.08	1.05	.28	.73	.12	1.11	.05	1.0	.12
C1	1.84	.06	1.22	.23	.87	.22			.91	.17
C2	1.27	.10	.74	.09	.79	.11	.95	.06	.51	.07
C3	1.10	.11	1.61	.09	1.49	.10	.65	.06	.60	.10
C4	.84	.08	.97	.05	.84	.10	1.31	.08	1.09	.13
D1	.96	.15	1.10	.12	1.29	.13	1.31	.05	.86	.03
D2	1.20	.02	1.11	.15	.67	.14			.57	.21
D3	.83	.07	.85	.09	.72	.15	.89	.10	1.29	.08
D4	1.11	.10	2.12	.03	1.62	.11			.86	.24
E1	.97	.13	.51	.14	.80	.05	1.30	.06	1.72	.09
E2	.91	.11	1.33	.09	1.51	.17	.88	.05	.91	.13
E3	.74	.08	.56	.10	.64	.10	1.68	.30	1.21	.09
E4	1.04	.14	1.80	.08	1.21	.11			1.79	.09
F1	.54	.13	.60	.26	.79	.13	1.16	.10	.88	.11
F2	.93	.08	.85	.11	.99	.03	1.56	.06	1.33	.23
F3	.93	.13	.91	.03	1.14	.09	1.26	.09	1.57	.21
F4	1.01	.09	.79	.13	.91	.08			1.05	.20

TABLE III   con't

AREA VI

SUBARRAY	AMP	ST DEV
A0	.76	.06
B1	.72	.03
B2	.58	.18
B3	.87	.19
B4	1.09	.15
C1	1.01	.08
C2	.61	.27
C3	.70	.16
C4	1.11	.09
D1	1.57	.10
D2		
D3	1.02	.14
D4	1.16	.06
E1		
E2	.82	.06
E3	2.35	.03
E4	1.52	.06
F1	.72	.13
F2	1.97	.11
F3	1.12	.18
F4	1.03	.17

Table IV

CORRELATION BETWEEN AMP AND RESIDUAL.

	Subarray	AMP	RES			Subarray	AMP	RES
Area 1	A0	.88	.13		Area 3	D3	.72	.03
	B1	1.35	.13			D4	1.62	.12
	B2	1.56	.18			E1	.80	-.07
	B3	.71	.07			E2	1.51	.08
	C1	1.84	.15			E3	.64	-.18
	C2	1.27	.12			E4	1.21	.11
	C4	.84	.04			F1	.79	-.03
	D2	1.20	.04			F3	1.14	0.0
	D3	.83	.02					
	D4	1.11	.06		Area 4	A0	.41	-.19
	E3	.74	-.16			B1	.53	-.17
	F1	.54	-.18			B3	.85	-.24
						B4	1.11	-.10
Area 2						C3	.65	-.22
	A0	.82	.11			C4	1.31	.02
	B1	.63	-.01			D4	1.31	.32
	B2	52	.13			E1	1.30	.39
	B3	1.26	.11			E2	.88	-.24
	C2	.74	.02			E3	1.68	.30
	C3	1.61	.16			F1	1.16	.29
	D3	.85	.02			F2	1.56	.22
	D4	2.12	.13			F3	1.26	.20
	E1	.51	-.13					
	E2	1.80	.12		Area 5	A0	.66	-.15
	F1	.60	-.07			B1	.57	-.19
	F2	.85	-.20			B2	.74	-.19
Area 3						C2	.51	-.22
	B1	.77	.16			C3	.60	-.20
	B2	1.51	.14			D1	.86	-.03
	B3	1.38	.09			D2	.57	-.26
	B4	.73	.01			D3	1.29	.07
	C2	.79	.04			E1	1.72	.35
	C3	1.49	.07			E3	1.21	.14
	C4	.84	.06			E4	1.79	.26
	D1	1.29	0.0			F2	1.33	.16
	D2	.67	-.09			F3	1.57	.13

Table IV (con't)

CORRELATION BETWEEN AMP AND RESIDUAL

	Subarray	AMP	RES
Area 6	A0	.76	-.06
	B1	.72	-.06
	B2	.58	-.21
	C2	.61	-.13
	C3	.70	-.20
	D1	1.57	.12
	D4	1.16	.31
	E2	.82	-.32
	E3	2.35	.15
	E4	1.52	.15
	F1	.72	.21
	F2	1.97	.07

FIGURE CAPTIONS

Fig. 1. Observed $dT/d\Lambda$ vs. for events located within the azimuth intervals of $295^\circ - 315^\circ$ and $135^\circ - 160^\circ$ measured from LASA.

Fig. 2. Observed travel-time minus predicted J-B travel time. The "X's" are for individual events from the southeast azimuths. Dashed lines as values obtained from integrating under the southeast-azimuth $dT/d\Lambda$ - vs -Λ curve after correcting the $dT/d\Lambda$ values as shown.

Fig. 3. Seismic velocity vs. depth obtained from inverting the $dT/d\Lambda$ values along the northwest and southeast azimuths.

Fig. 4. Comparison of $dT/d\Lambda$ - vs -Λ curves for two upper mantle velocity models. One is cit.11; the other is from Chinnery and Toksöz (1966). Lower mantle velocities (below 650 Km) are those shown on Fig. 3 for the northwest azimuth.

Fig. 5. Comparison of horizontal phase velocities measured at TFSO (Johnson, 1966) and LASA.

Fig. 6. Average plane wave residual at each subarray for northwest - azimuth events. Standard deviation of average is about 0.05 seconds. Different symbols represent distance increments. Abscissa is distance between subarray and array center projected onto azimuth line of 310°.

Fig. 7. Average quadratic wave residuals for northwest - azimuth events plotted in same manner as Fig. 6.

Fig. 8. Average plane wave residual for southeast azimuth events plotted in same manner as Fig. 6. Abscissa is distance between subarray and array center projected onto azimuth line of 145°.

Fig. 9. Average quadratic wave residual for southeast azimuth events plotted in same manner as Fig. 8.

FIGURE CAPTIONS

Fig. 10. Average plane wave residuals vs. relative
amplitude for northwest - azimuth events.(Table 3).
Different symbols represent distance increments.

Fig. 11. Average plane wave residuals vs. relative
amplitude for southeast-azimuth events (Table 3).
Different symbols represent distance increments.

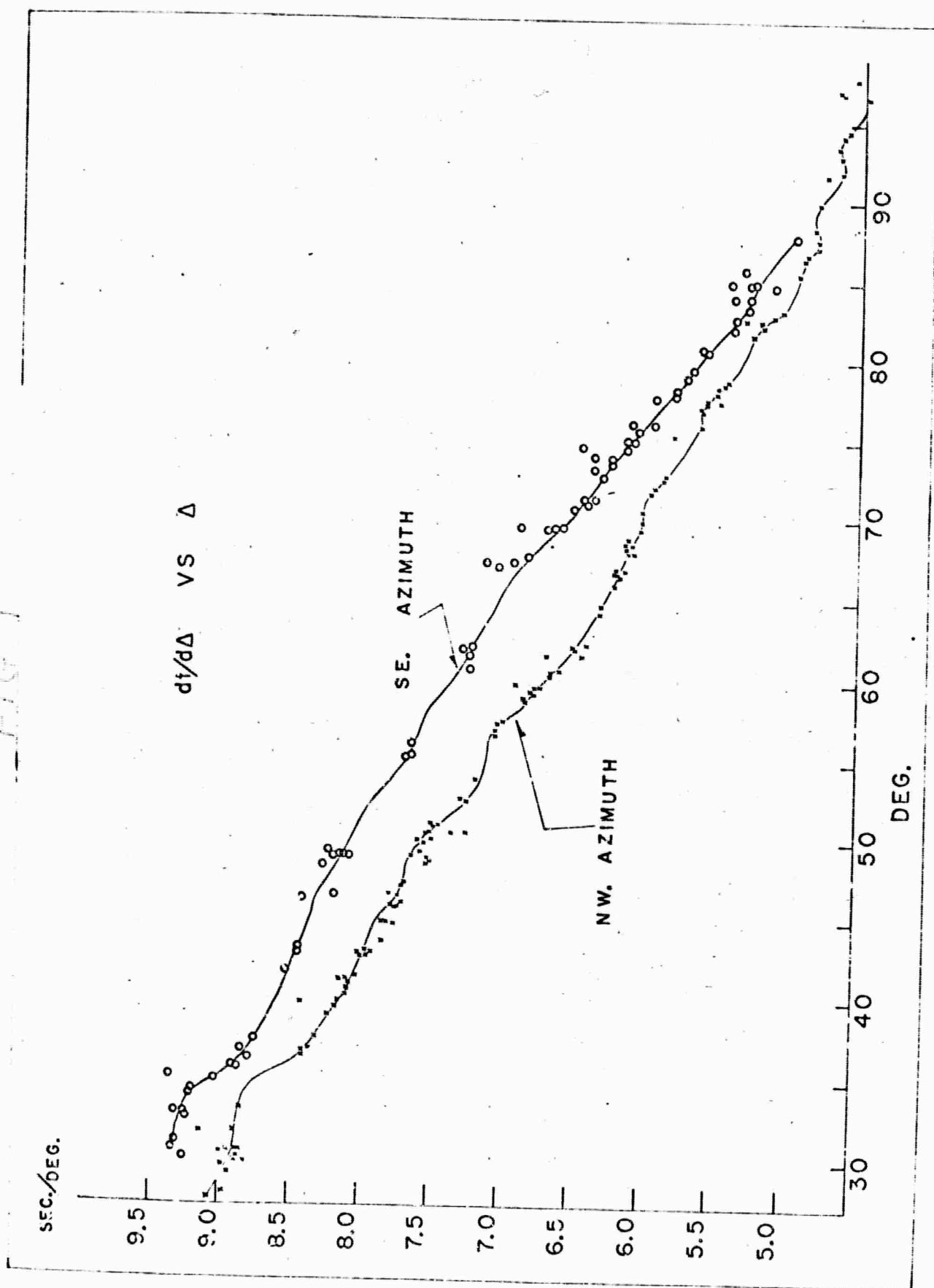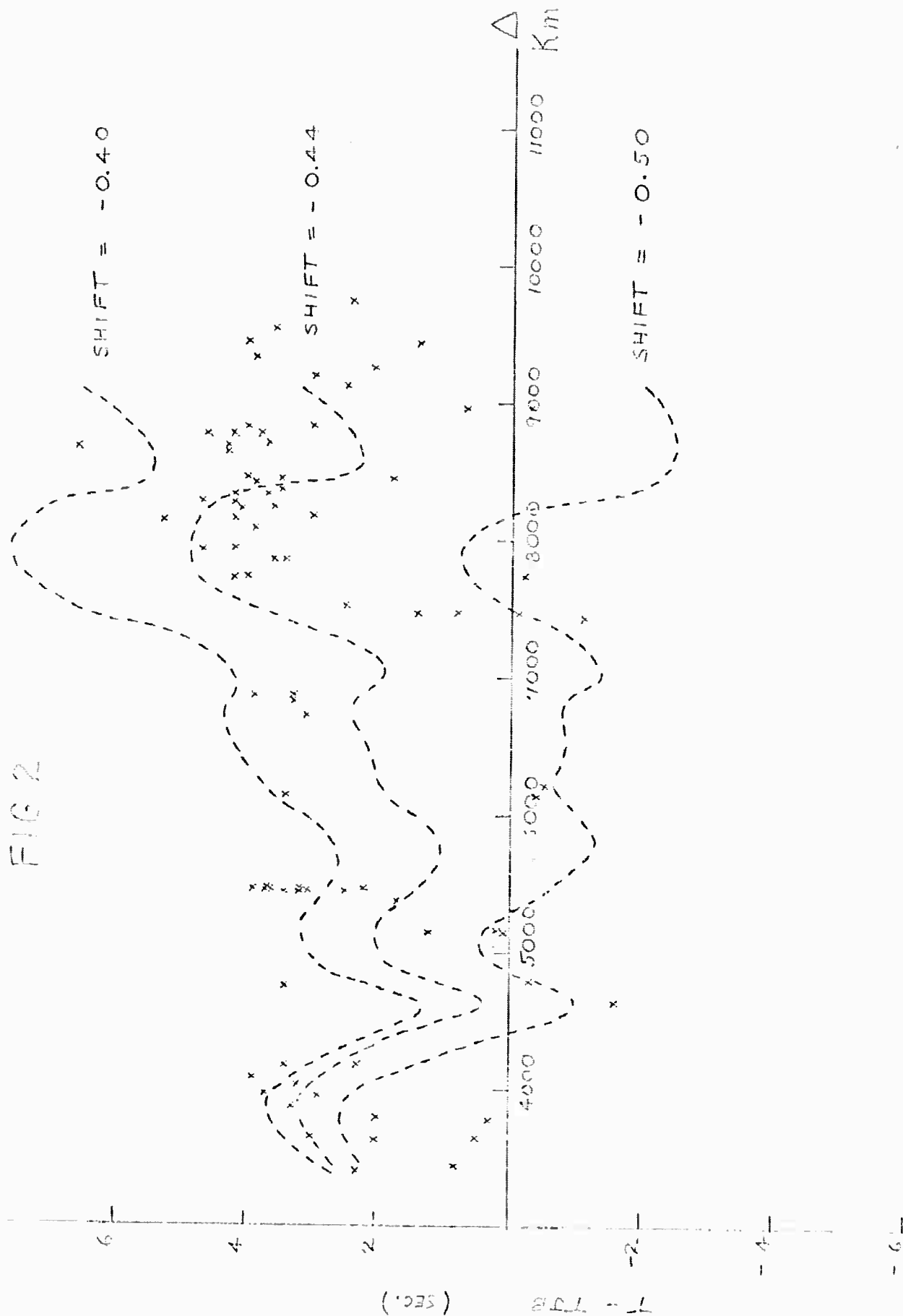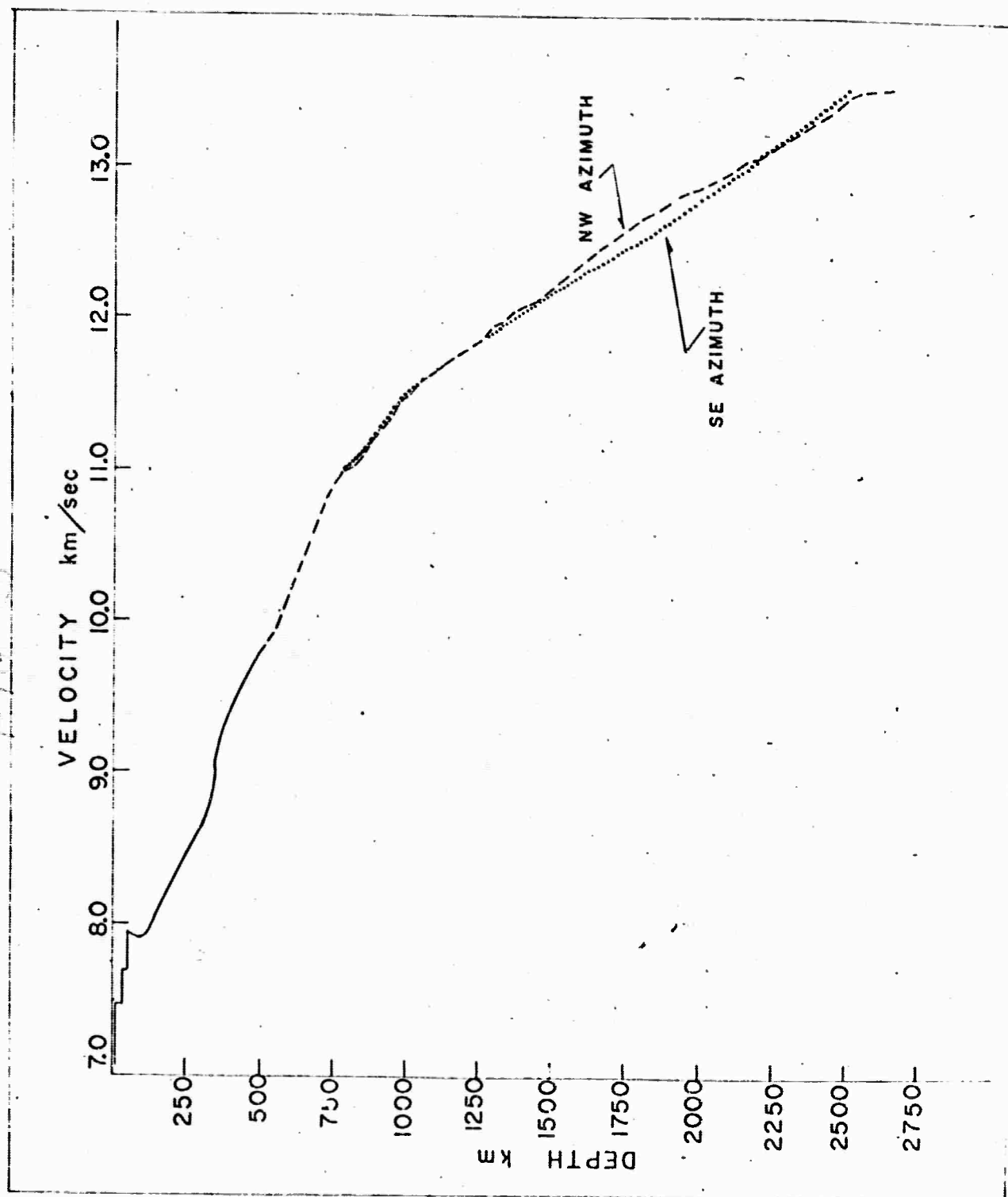Fig. 12. Diagram of LASA showing the location of the
21 subarrays.

FIG. 1

$d\dagger/d\Delta$ VS Δ

SE. AZIMUTH

NW. AZIMUTH

SEC./DEG.

DEG.

FIG 2

FIG 3

FIG 4

X   CIT 11
O   CHINNERY AND TOKSÖZ
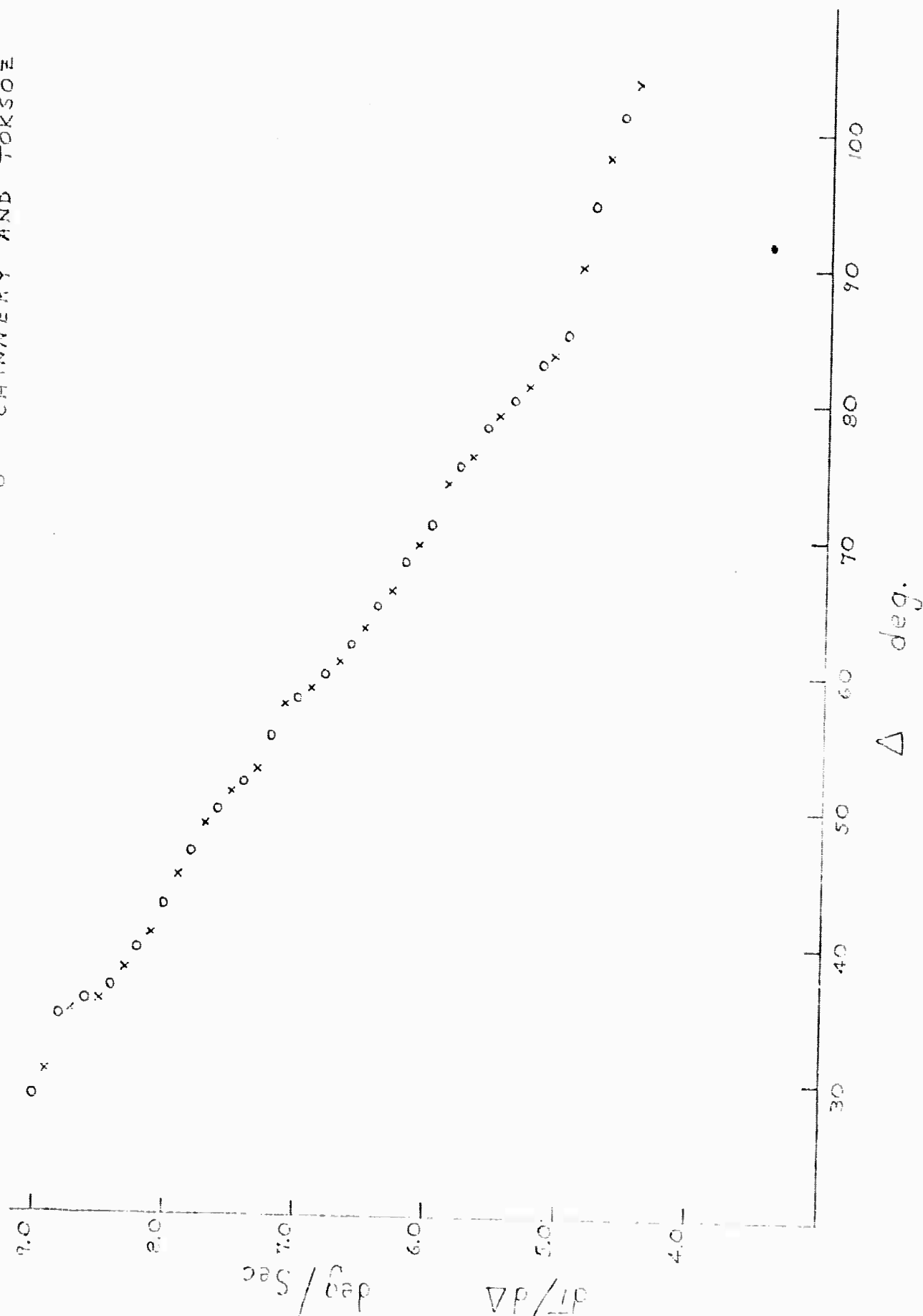
FIG 5

‒ ‒ ‒   TFO
X X X   LASA, SOUTHEAST
O O O   LASA, NORTHWEST
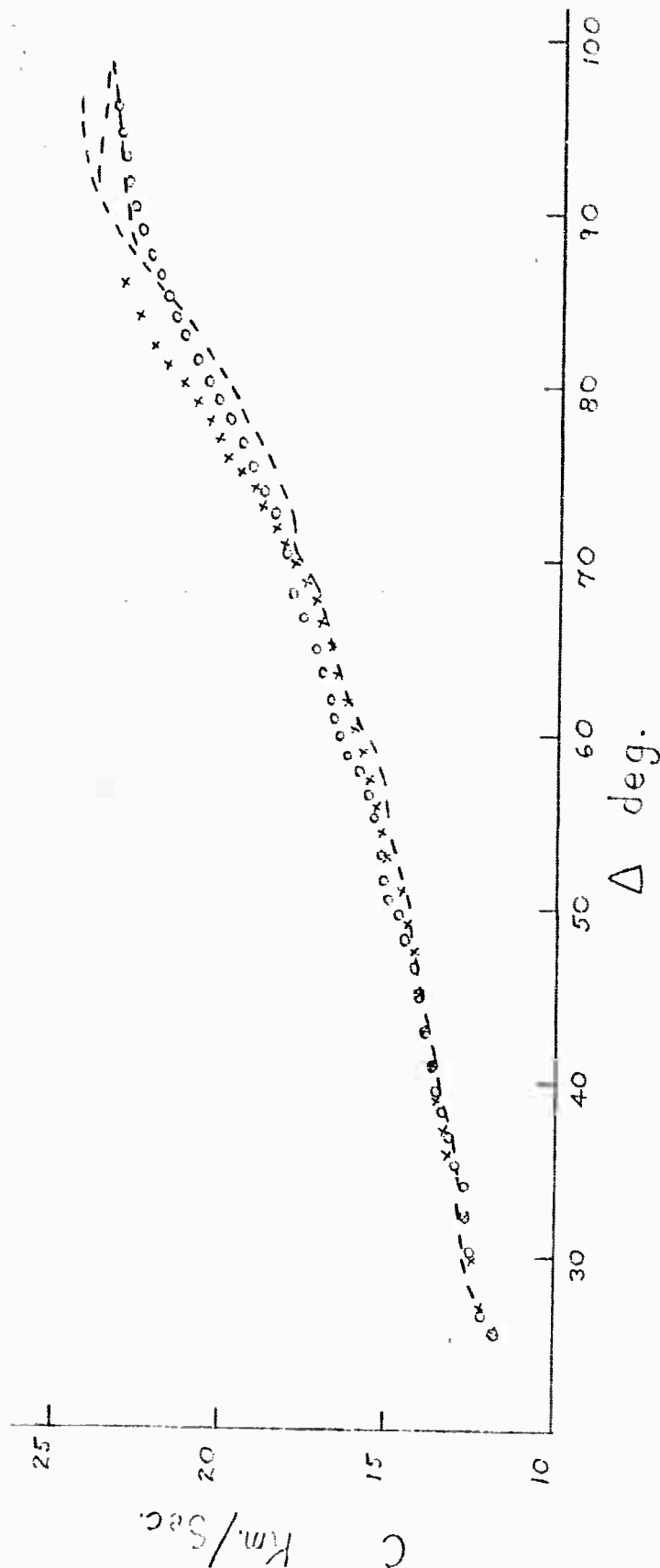
Δ deg.

C Km/Sec.

FIG. 6
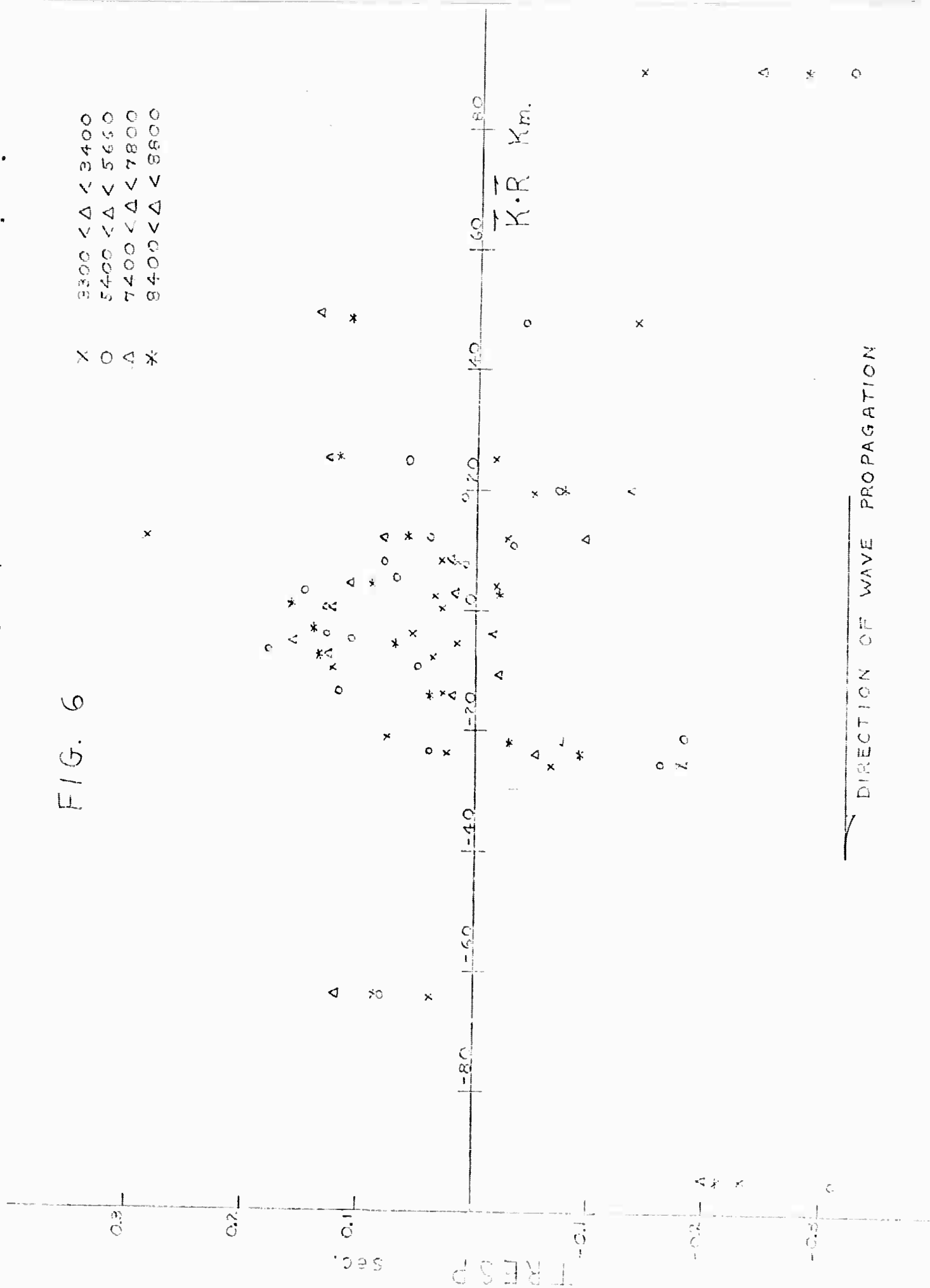
DIRECTION OF WAVE PROPAGATION

FIG 7
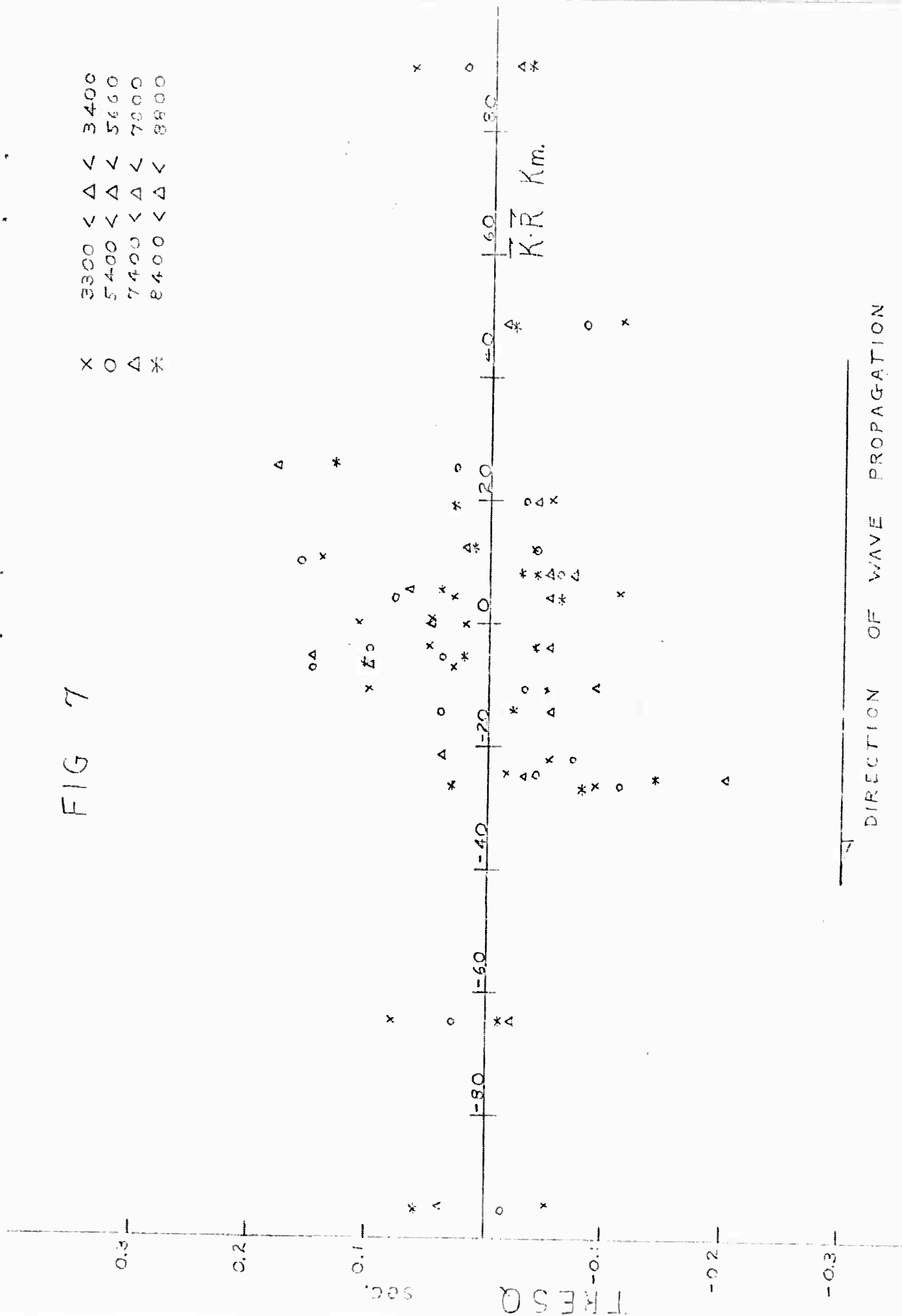
DIRECTION OF WAVE PROPAGATION

FIG 8
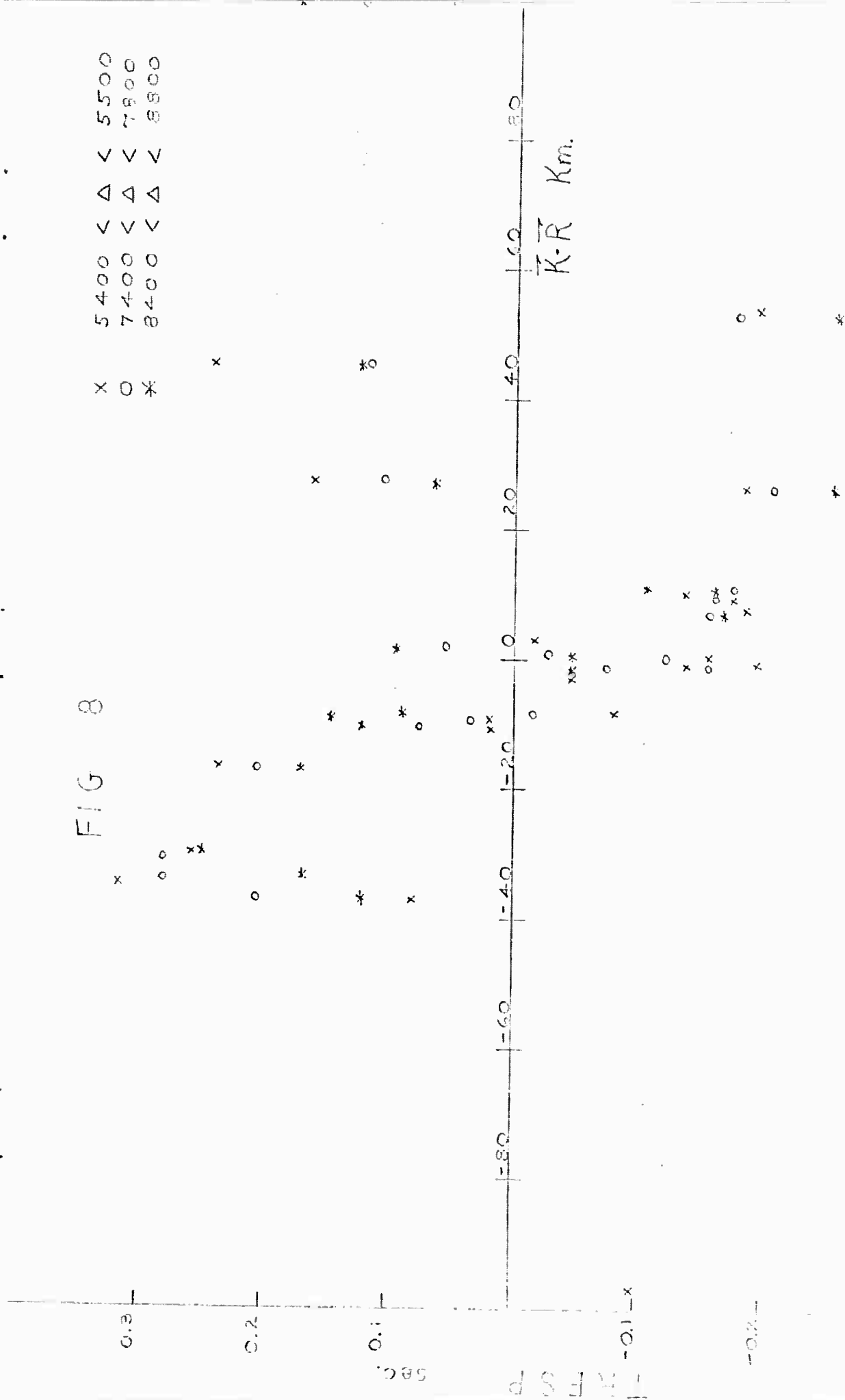
DIRECTION OF WAVE PROPAGATION

$\overline{K \cdot R}$ Km.

T.F.S.P. sec.

FIG 9

×	5400 < Δ < 5500
O	7400 < Δ < 7800
✳	8400 < Δ < 8800
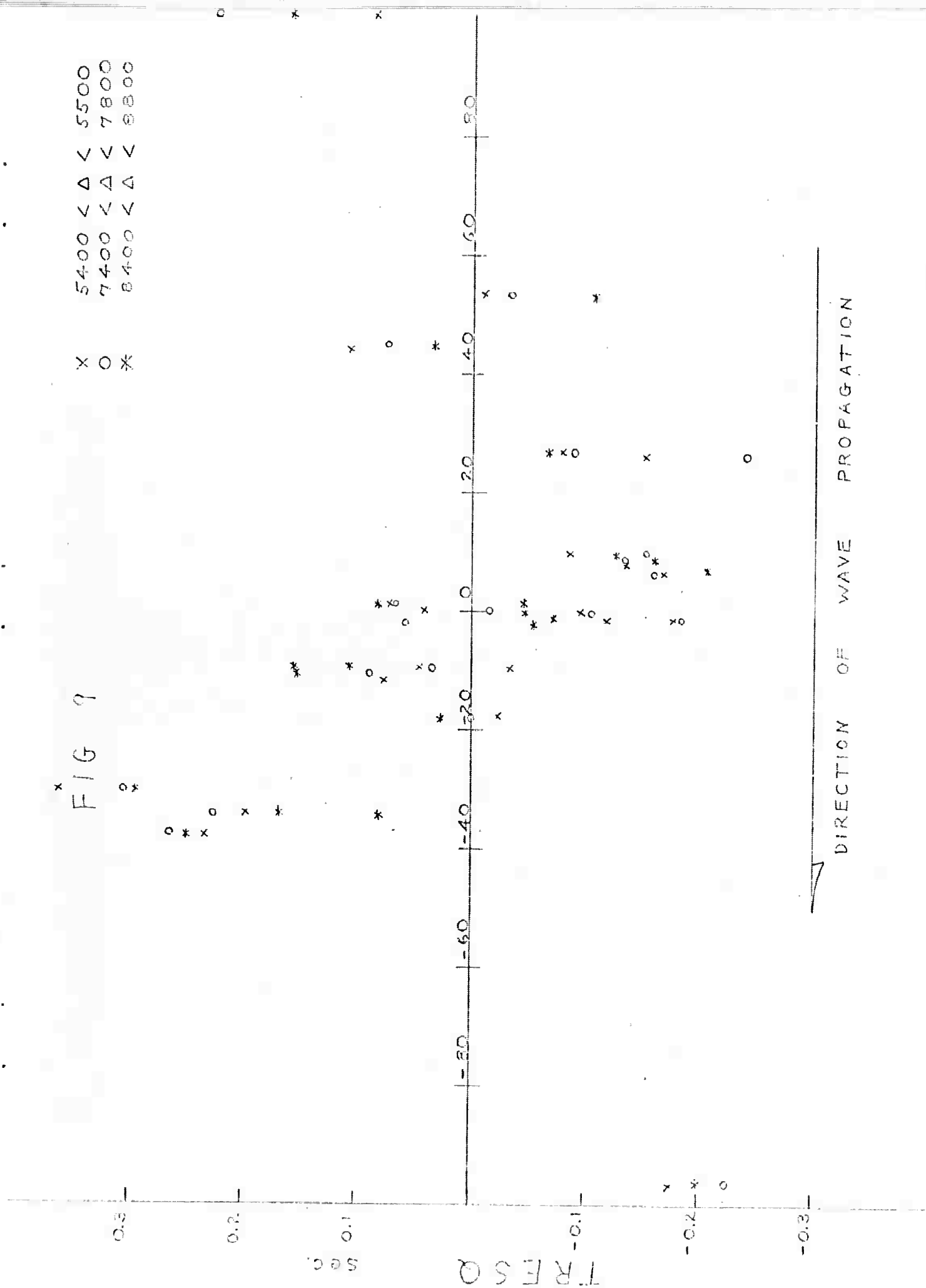
TRESO sec.

DIRECTION OF WAVE PROPAGATION

FIG 10

RELATIVE
AMPLITUDE

X   5400 < △ < 5460
O   7400 < A < 7450
△   8400 < △ < 8750

2.0

1.5

1.0

0.5

0.3

0.2

0.1

-0.1

-0.2

-0.3

T R E S P   sec

FIG. 11
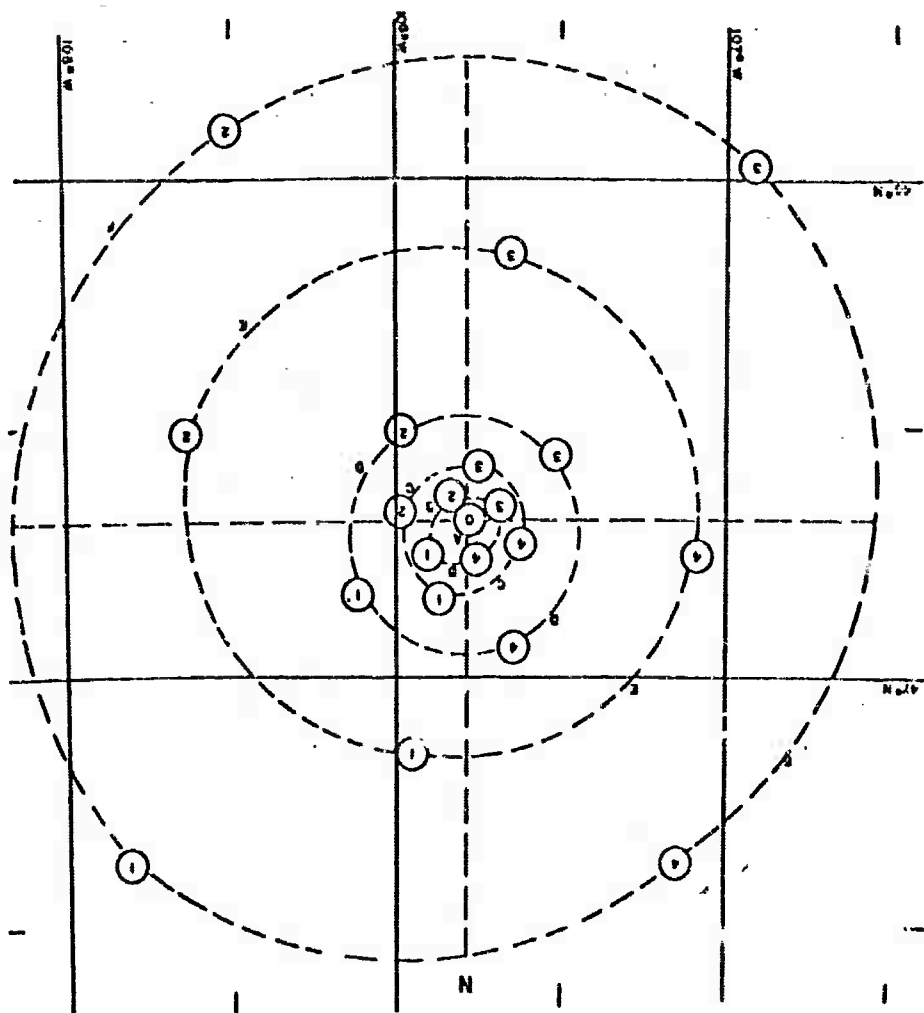
RELATIVE AMPLITUDE

TRESP sec.

SUB-ARRAY "AO"
46° 41', 13" N
106° 13', 20" W

0 10 20 30 40 50 KM

N
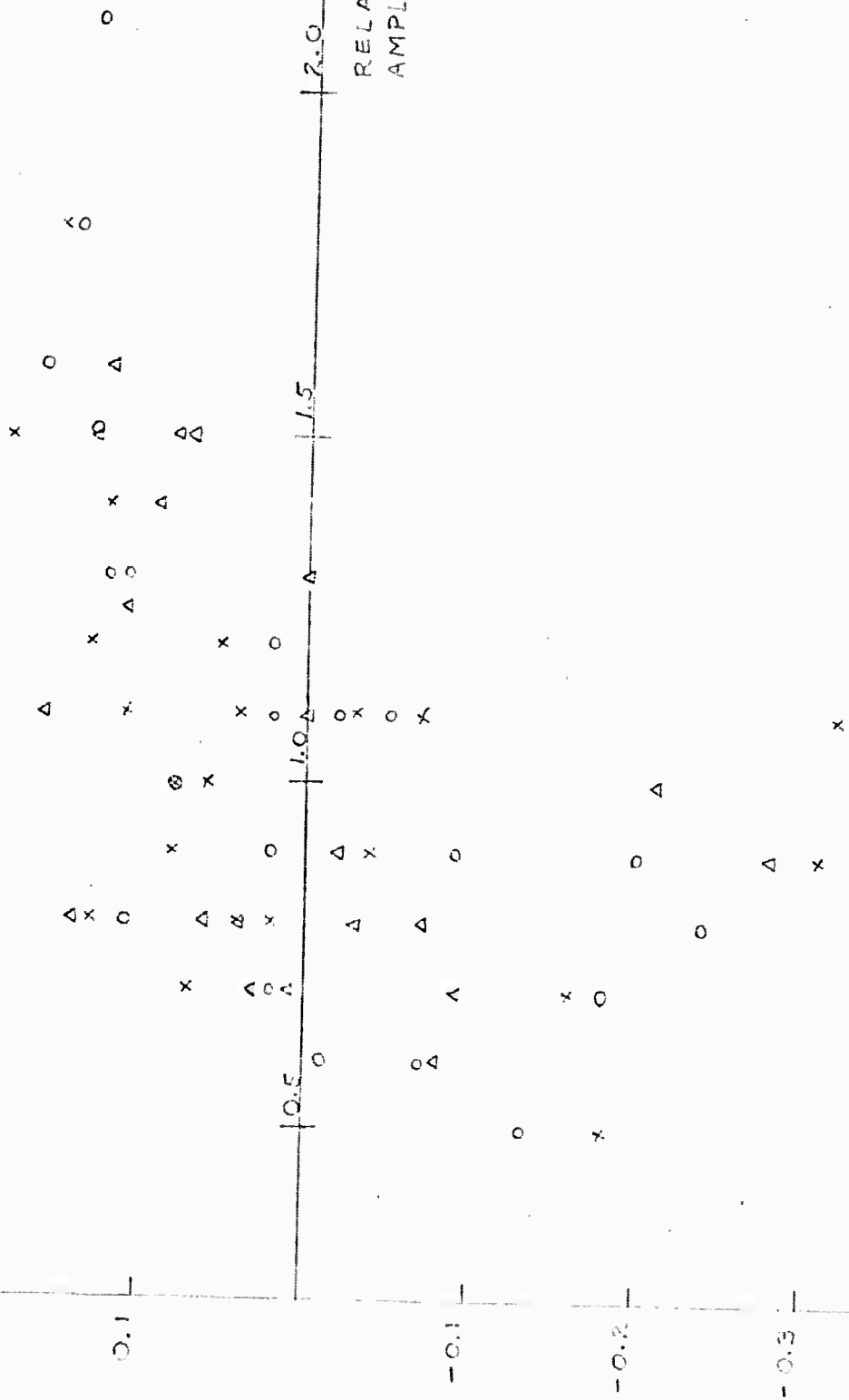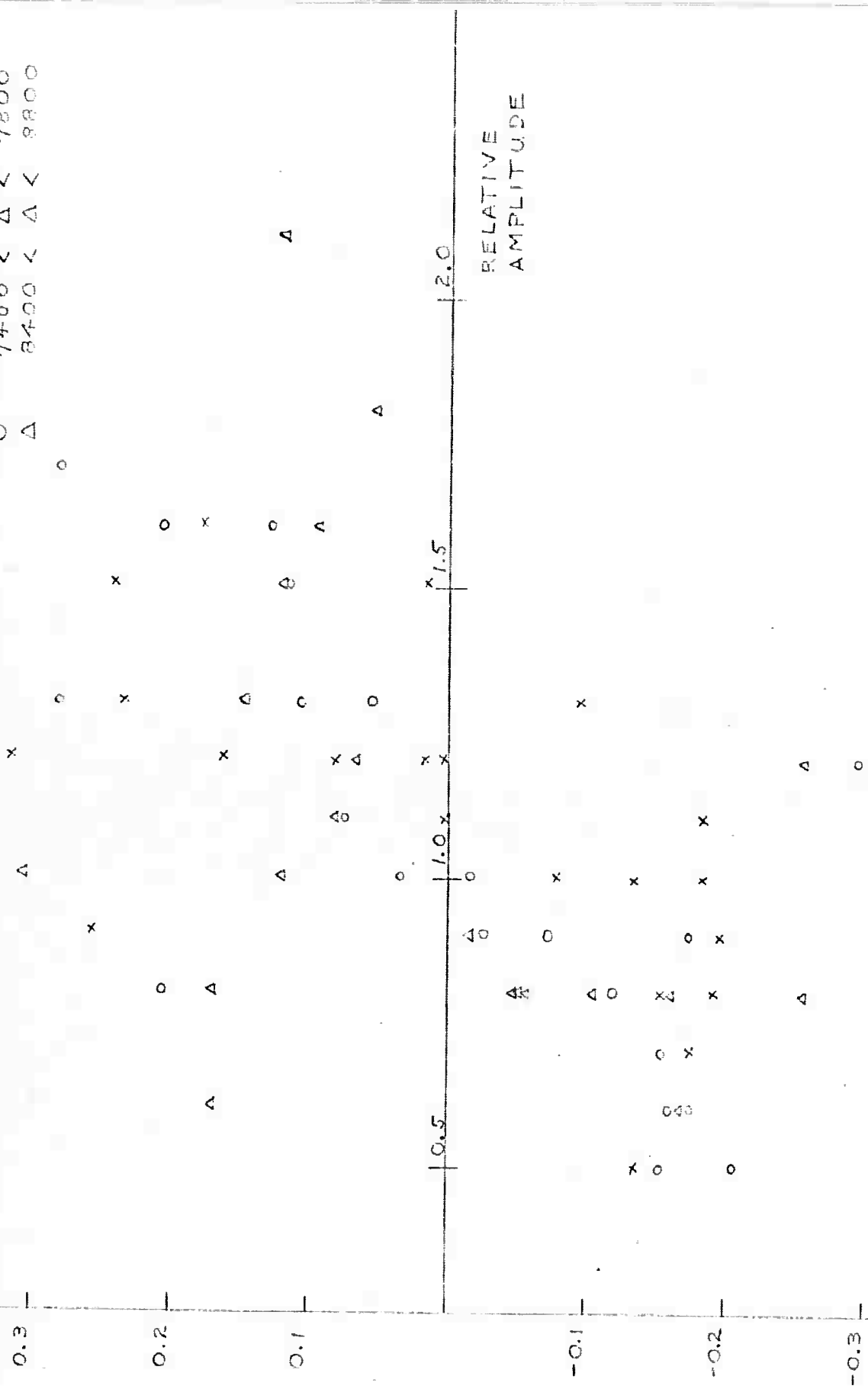
II.2. Mode Structure and Source of Microseisms

In this study we have investigated the mode structure of microseisms using the Large Aperture Seismic Array (LASA) in Montana. LASA consists of 525 short period vertical and 21 three-component long period seismometers and it provides the desired large aperture and seismometer density for wavenumber resolution over a very broad frequency range. Furthermore, the availability of horizontal seismometers enables us to investigate both the Rayleigh and Love wave components of the long-period microseisms.

We consider the microseisms as a random process, stationary in time and space over a time interval equal to the sample length. We then compute the three-dimensional Fourier transform of the correlation function of space and time variables. The result gives power spectral density in frequency wavenumber space. In other words, with this process we can obtain the power at each frequency as a function of phase velocity and direction of approach.

For the investigation of short period (shorter than 5 seconds) microseisms sets of 28 and 36 vertical short-period seismometers were used for forming beams. These were chosen to provide a fairly uniform spatial coverage. Microseism records of 6 to 12 minutes duration were analyzed on different

days. The results of a typical day are shown in Figures 1 and 2. These are plots of the power level (relative to peak power) at each frequency as a function of east and north components of the wavenumber. In these figures the origin corresponds to zero wavenumber or infinite phase velocity. At a given frequency f, the increasing wavenumber k will mean a lower phase velocity c since these quantities are related by $c = \frac{f}{k}$. At f = 0.2 cps in Figure 1, we see a power peak in the NE quadrant. This corresponds to a direction of approach of microseisms to LASA from about N 50° E with a phase velocity of about c = 3.5 km/sec. At f = 0.3 cps, in addition to the previous peak, an arrival from the west and with much greater phase velocity becomes apparent. In Figure 2, these peaks are outlined with greater resolution, and it is found that the waves arriving from the west have a phase velocity of about 13.5 km/sec. At higher frequencies (f = 0.4, 0.6 cps) we observe the disappearance of the low velocity peak and the prominence of the two well-defined high velocity peaks.

Seismic waves having such high (13.5 km/sec) phase velocities correspond to compressional body waves. Thus with the prominence of these high velocity peaks we can conclude that, for this particular example, the high frequency microseisms recorded at LASA consist predominantly of seismic P waves. The peak at f = 0.2 cps and c = 3.5 km/sec corresponds to first or second higher Rayleigh mode. The Rayleigh wave dispersion curves for a preliminary LASA structure are shown in Figure 3.

The analyses of short period microseism data recorded at other days show similar results. These are summarized in Figures 4 and 5 for arrivals from easterly and westerly directions. Each point corresponds to a peak in the frequency-wavenumber diagrams such as Figure 2. From the grouping of the data, it is clear that we can identify two modes of propagation: (1) the high-velocity body waves and (2) the low-velocity surface waves. As can be seen from Figure 3, the surface waves again correspond to higher Rayleigh modes. rather then the fundamental modes.

At long periods, microseisms were analyzed using similar techniques with longer time samples and a subset of the 21 three-component seismometers. The frequency-wavenumber results for the vertical components of the motion are summarized in Figure 6. This dispersion curve corresponds to that of a fundamental mode Rayleigh wave. Thus we can conclude that at periods longer than about 6 seconds, the vertical component of microseismic motion is due to fundamental mode Rayleigh waves.

The presence of Love waves in long period microseisms is also observed for one of the microseismic peaks. After the main source of energy was determined a beam was formed, and the horizontal seismometer outputs were combined to form purely radial and transverse components of the motion. The elements of the cross spectral matrix at $f = 0.065$ cps are listed in

in Table 1. Here we observe that the vertical and radial
motion are approximately equal and highly correlated with a
phase difference of 90°. This corresponds to retrograde
Rayleigh motion and hence to fundamental Rayleigh mode. The
transverse component, larger than the radial by a factor of
two, is not correlated with the radial or the vertical motion.
It corresponds to a Love wave, coming from the same direction
as the Rayleigh wave. Since there were no other prominent
peaks in the frequency-wavenumber diagram for that time, this
transverse motion cannot be due to Rayleigh waves arriving
from a different direction.

Before undertaking the problem of generation mechanism
of microseisms let us summarize the results: On a typical
day the microseisms recorded at Montana consist of both body
waves and multi-mode surface waves. At frequencies higher
than 0.3 cps most of the microseisms consist of compressional
body waves. In the frequency range of 0.2 and 0.3 cps both body
waves and higher mode Rayleigh waves are observed, with the
relative power of surface waves increasing with decreasing
frequency. At frequencies below 0.15 cps the microseisms consist
primarily of fundamental mode Rayleigh waves. Appreciable
amounts of fundamental mode Love wave energy may also be present
at these low frequencies. These results constitute very
comprehensive data about the mode structure and the composition
of the microseisms. They cover a very broad frequency range
from 0.04 cps to 0.6 cps, and provide a greater resolution than
any of the earlier studies.

We need to clarify one point about the above results.
They apply to LASA and probably to the interior regions of the
continents. At coastal regions and near great lakes fundamental
mode Rayleigh waves may be present even at higher frequencies
providing these can be generated nearby. We would not expect
short period surface waves to propagate over great distances
from source regions since such waves attenuate rapidly due to
crustal inhomogeneities and surface irregularities.

Frequency-wavenumber diagrams such as Figures 2 and 3
enable us to determine directly the source of the body-wave
component of microseisms. These provide the direction and the
phase velocity of the body-wave, and the source regions can be
determined from the projected ray paths. These are shown in
Figure 7. They are in the Labrador Sea and in the Pacific Ocean.
These areas correspond to stationary low-pressure regions on
the weather map for the same data and two previous days. Thus,
we can conclude that the body waves in microseisms are due
to the atmosphere-ocean interaction and the resulting pressure
fluctuations at the ocean bottom. These pressure fluctuations
have been observed with ocean-bottom instruments. By correlating
weather maps, ocean waves and microseisms, other studies have
shown that the source of low frequency microseisms is also
the coupling of energy between water bodies, such as oceans,
and the earth's crust.

The Love waves cannot be excited by pressure fluctuations at the ocean bottom. They must be due to either the conversion of Rayleigh waves to Love waves along complicated propagation paths, or to surf action or other motions where shear forces are exerted on the solid medium.

the contribution of very small earthquakes, creep action, and other dislocations in the earth's crust to the observed microseisms seems to be very small, if any. In our frequency-wavenumber studies we could not find power peaks pointing in the directions of the seismically active regions of the earth.

Reference:

Toksöz, M. N. and R.T. Lacoss, Microseisms: Mode structure and sources, Science, 1968 (in press).

FIGURE CAPTIONS

Figure 1. Wavenumber structure of microseisms on 2 December 1965. Divisions on coordinate axis are in units of 0.05 cycle/km.

Figure 2. Wavenumber structure of microseisms on 2 December 1965. Axis scales are same as in Figure 1.

Figure 3. Rayleigh wave dispersion curves for an average structure of LASA.

Figure 4. Cumulative frequency-wavenumber plot of microseism power peaks arriving from the east. Note the separation of surface waves and body waves on two sides of 8 km/sec line.

Figure 5. Frequency-wavenumber plot for microseisms arriving from the west.

Figure 6. Frequency-wavenumber dispersion curve for the long period vertical motion of microseisms. The points corresponds to the fundamental mode Rayleigh wave dispersion.

Figure 7. Source regions of microseisms recorded at LASA on 2 December 1965. Dotted areas are the regions where body waves originated.
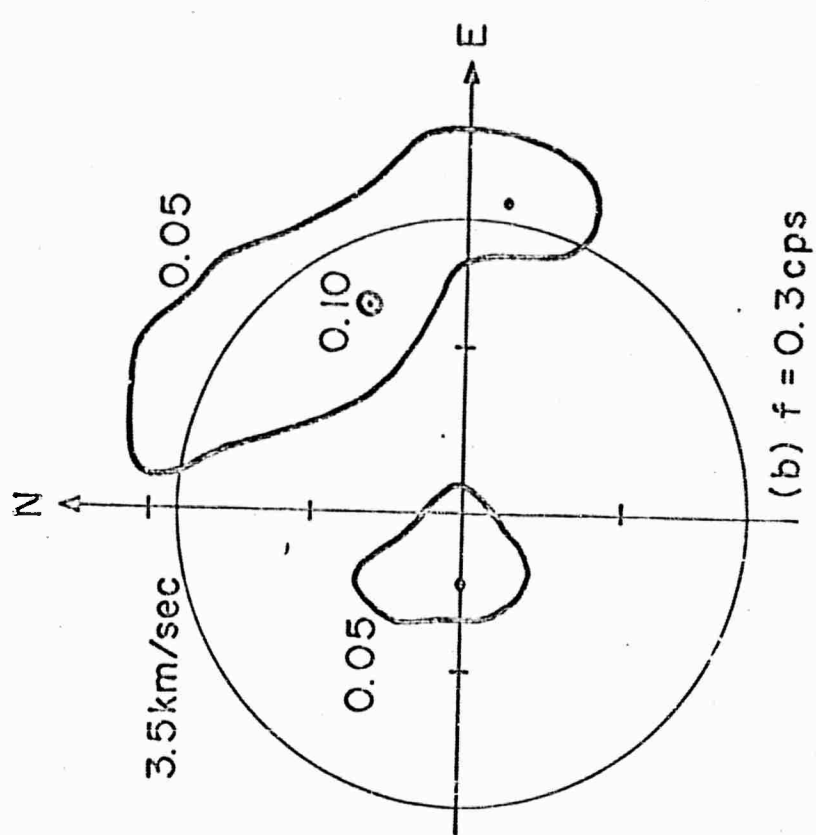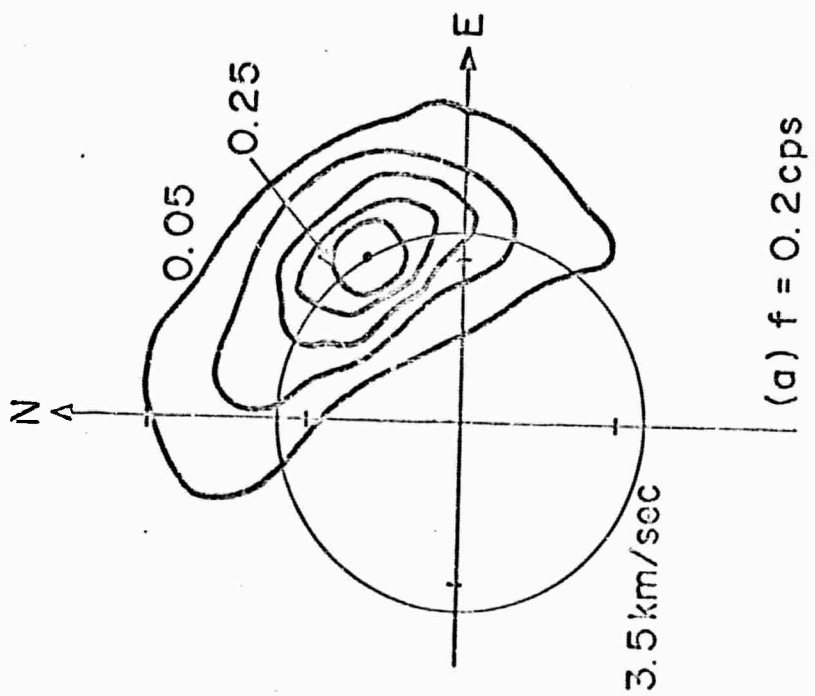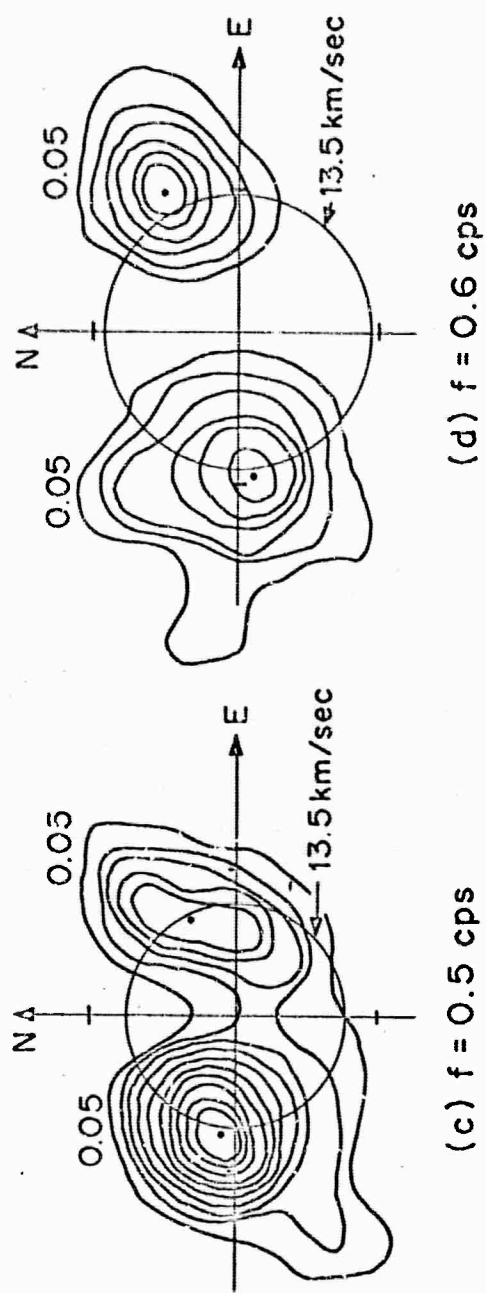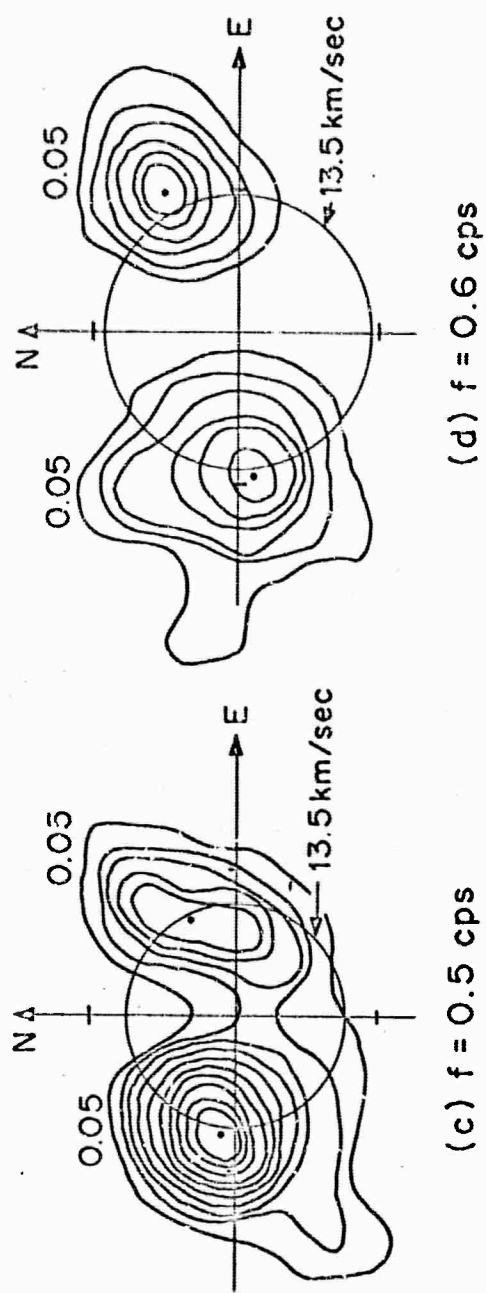
(a) f = 0.2cps

(b) f = 0.3cps

Fig. 1

(a) f = .0.3 cps

(b) f = 0.4 cps

(c) f = 0.5 cps

(d) f = 0.6 cps

Fig. 2

Fig. 3

Fig. 4

WAVE NUMBER (cycles / km)

FREQUENCY (Hz)

8km/sec
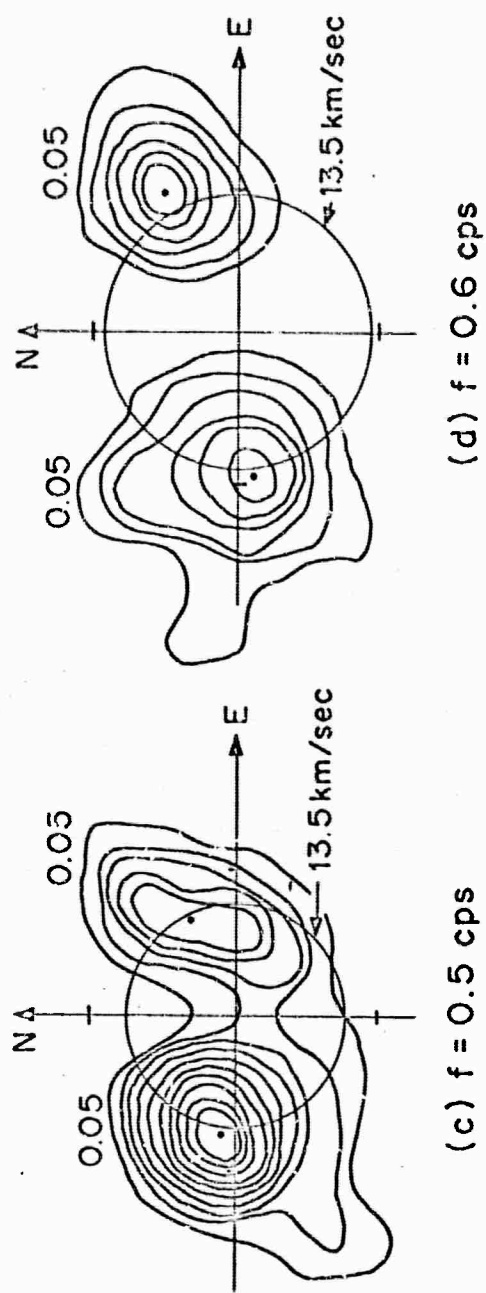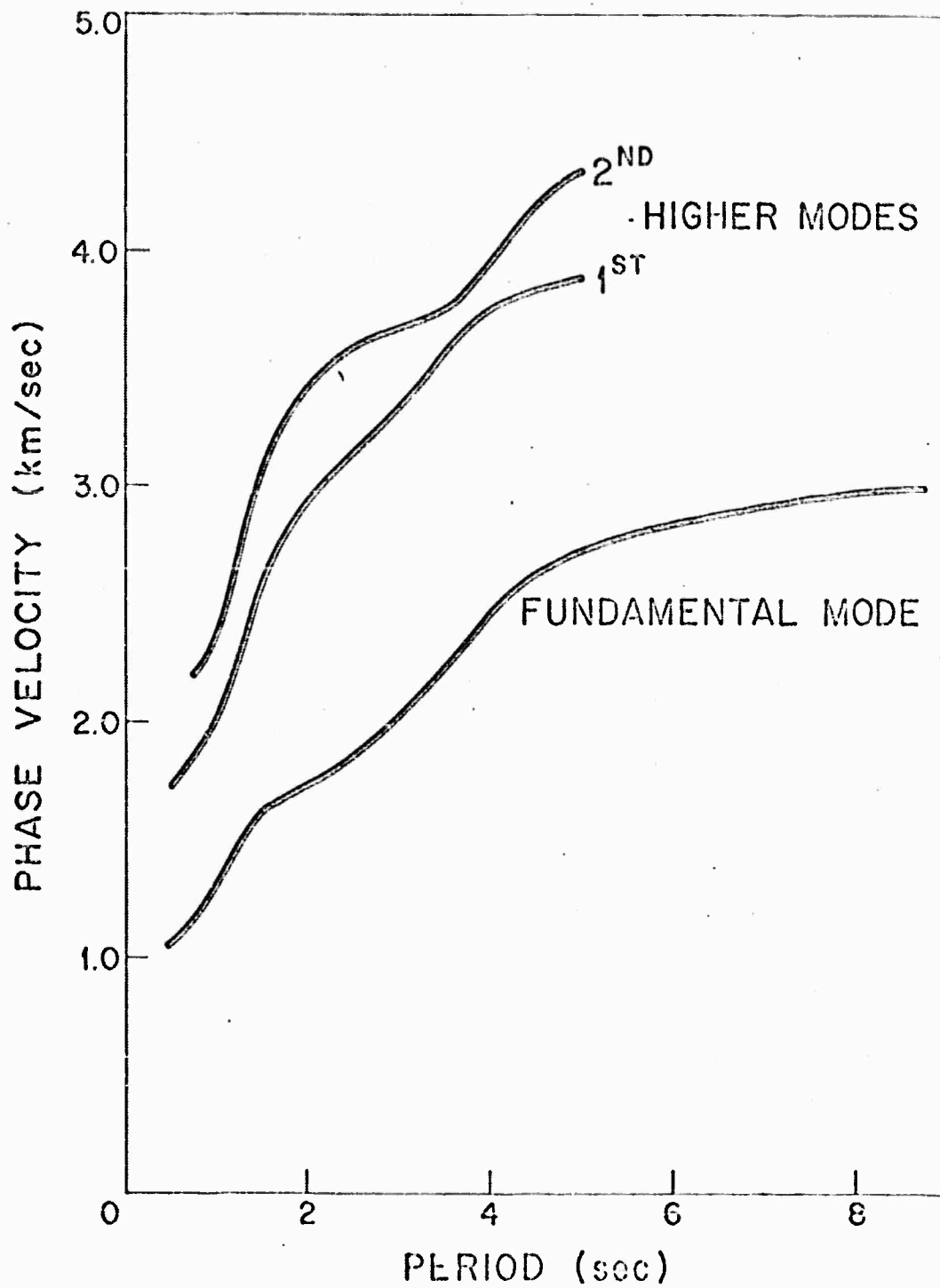
Fig. 5

Fig. 6

Fig. 7

II.3.   Rayleigh Wave Particle Motion

                          and Crustal Structure

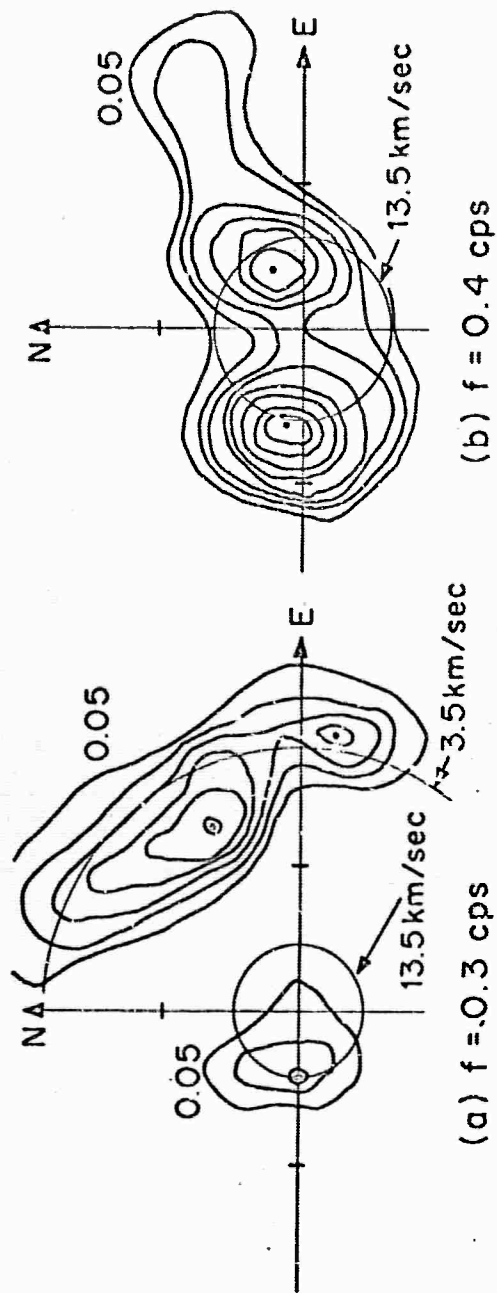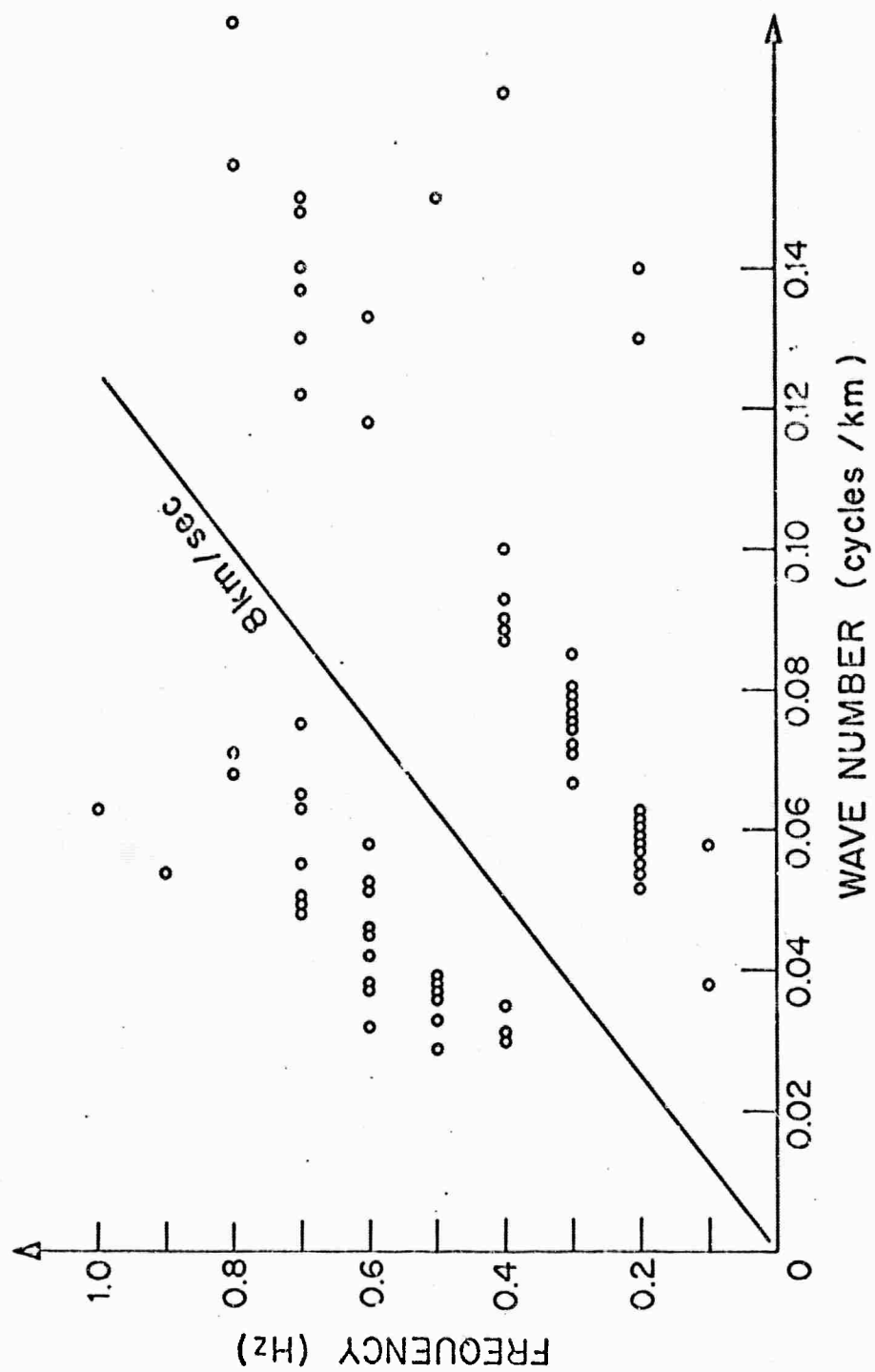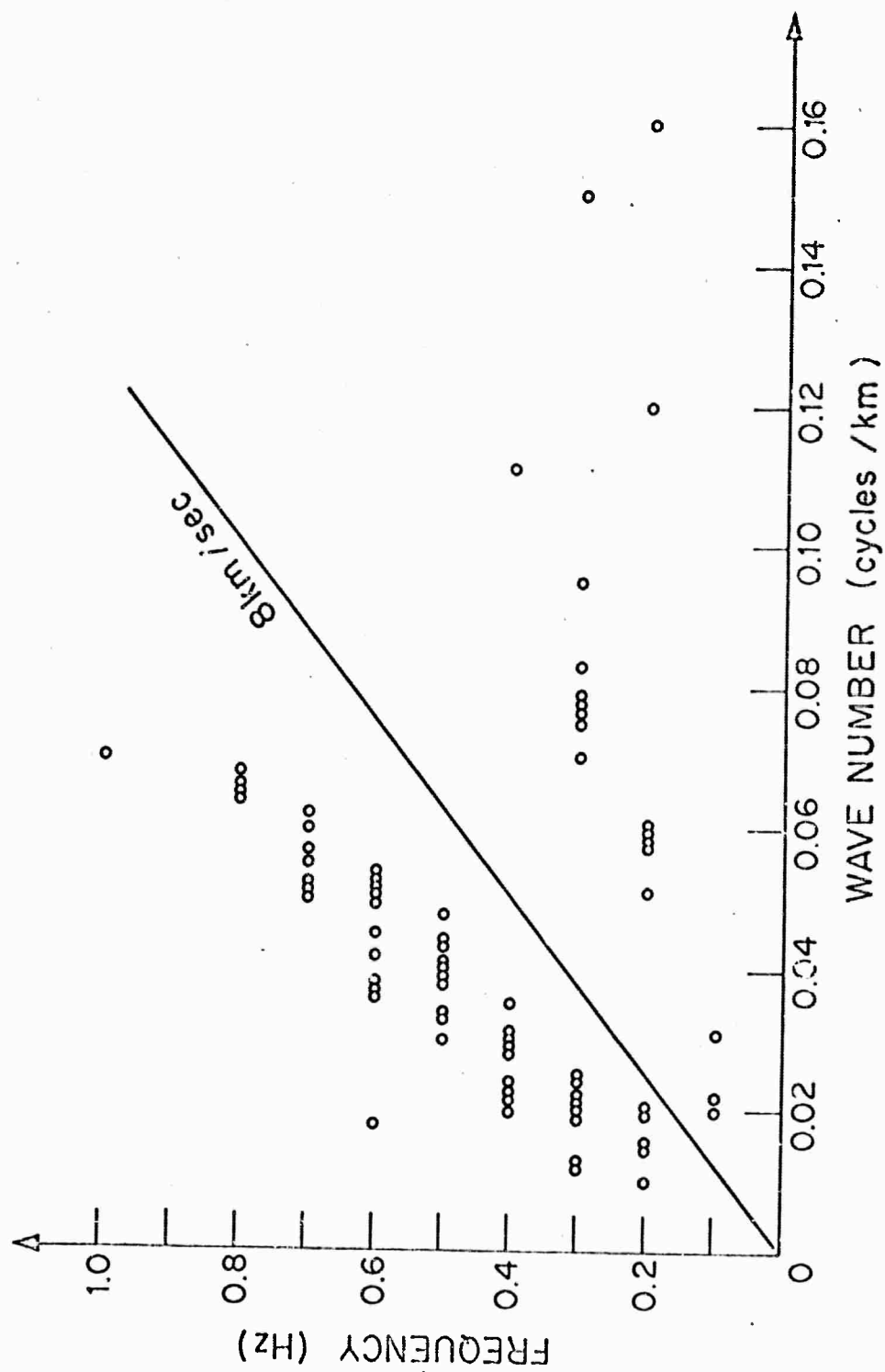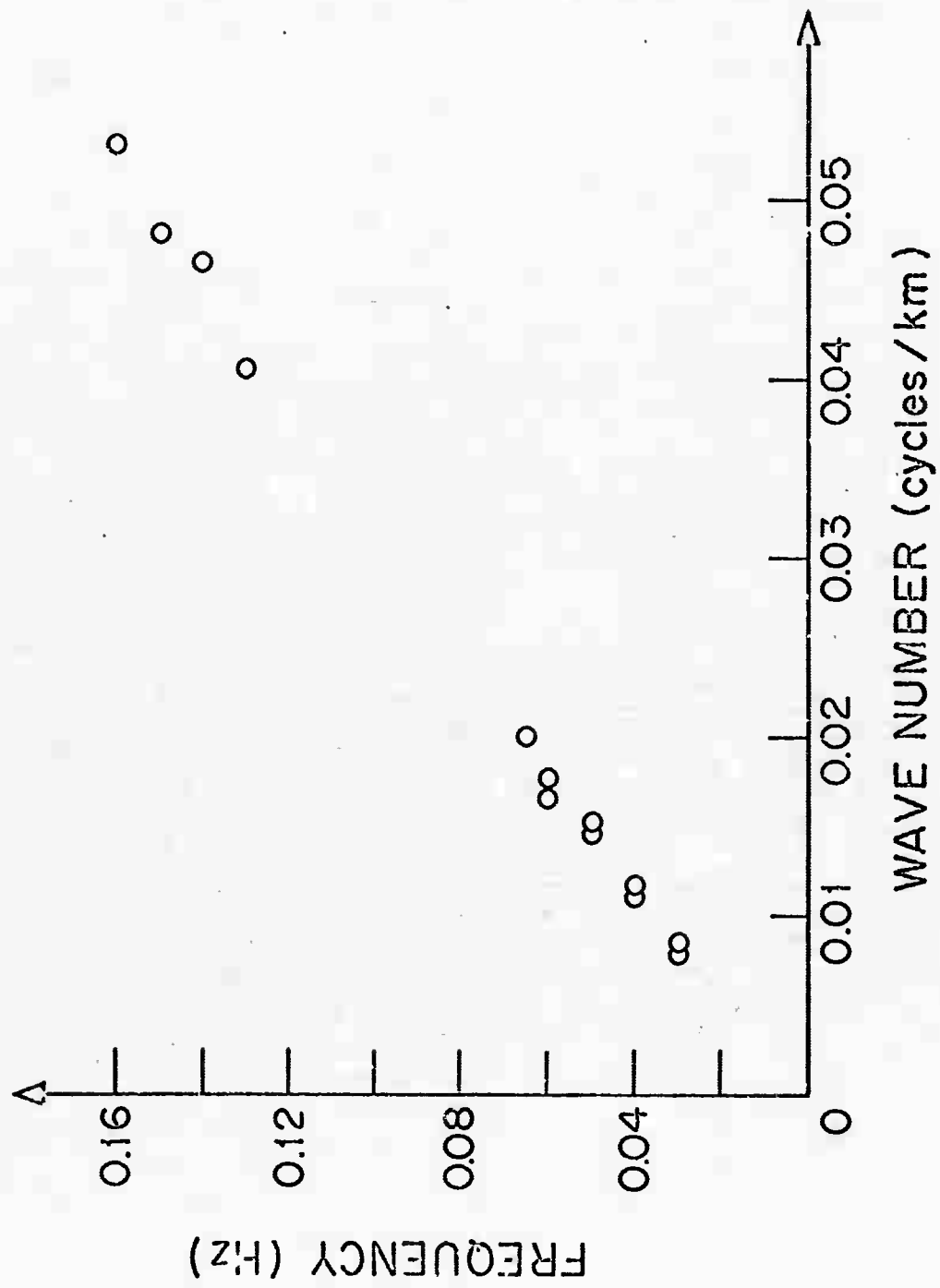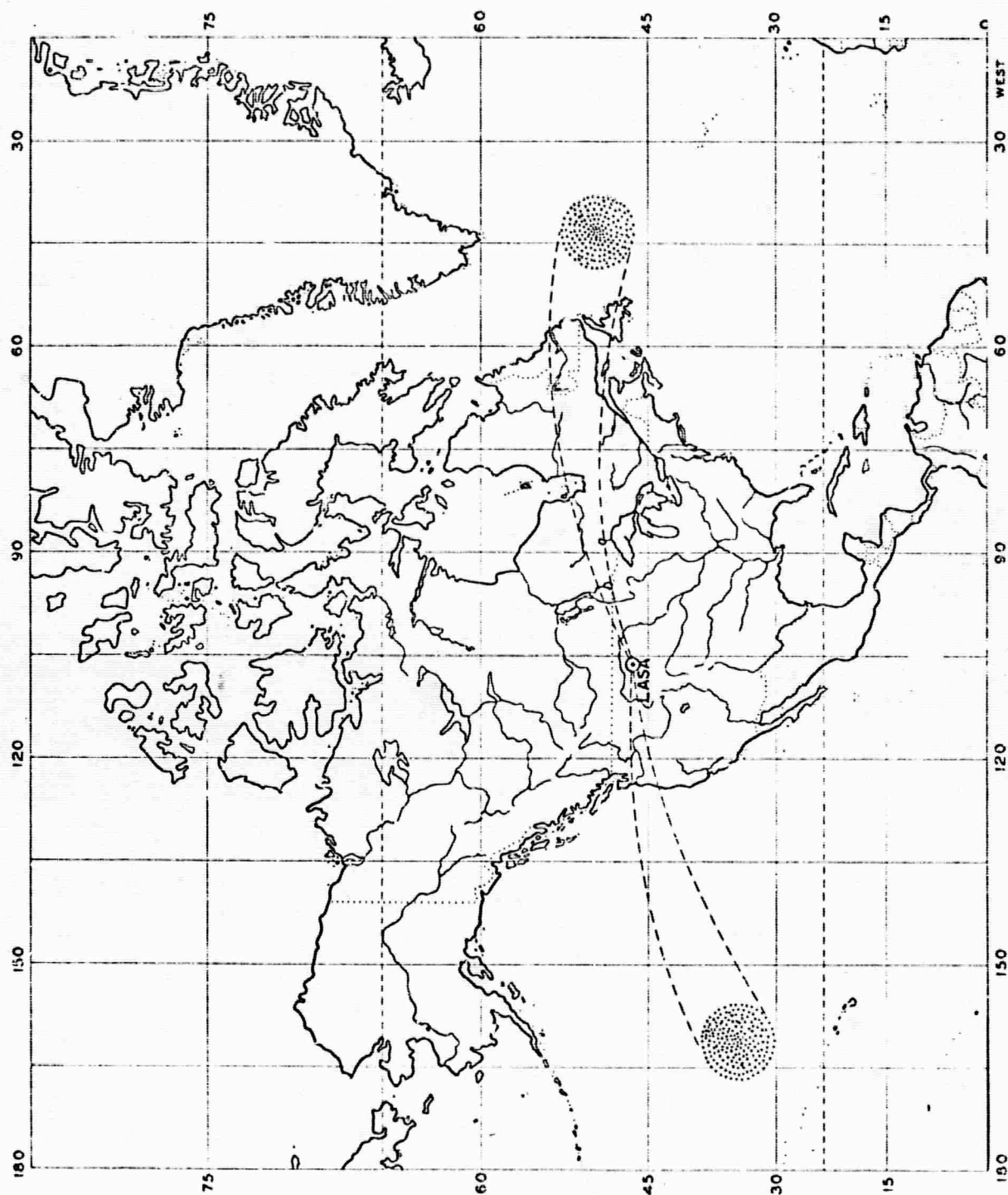The study of phase and group velocity of seismic surface waves has led to important contributions in our understanding of the earth's crust and upper mantle. In this study the use of ellipticity of the Rayleigh wave motion to determine the structure is investigated. Although this method is theoretically feasible, its practicality is tested using data from long period instruments at LASA.

For far-field distances ($kr \gg 1$) from an arbitrary point source in a perfectly elastic layered medium Haskell (1964) gives the following expression for the ratio of the radial and vertical components of Rayleigh-wave particle motion:

$$\frac{U_{HR}}{U_V} = -\frac{i\omega}{c(\omega)} \left[\frac{J_{11} - J_{22}}{J_{11} - J_{21}} \right] \tag{1}$$

where ω=frequency, $c(\omega)$=phase velocity, $J_{11} \cdots J_{21}$ are real matrix components involving the layer parameters (density, compressional and shear velocities, and thickness), frequency, and phase velocity. U_{HR}, U_V=spectra of the radial and vertical components of motion, respectively. This expression shows that the spectral ratio of the displacements (the absolute value of which will hereafter be termed "ellipticity") is purely imaginary, indicating that the vertical and radial displacements are 90° out of phase, and depends only on frequency and layer parameters. The expression holds for any order mode. Thus a plot of ellipticity versus frequency will be similar to a dispersion curve. The advantages over phase

velocity are that only one station is needed and that the computed structure is a more local average than that obtained from phase velocity measurements.

Numerical studies show that ellipticity is, in general, as sensitive to parameter changes as phase velocity. In the period range of 15-60 seconds, however, it is much more sensitive to surface sedimentary layers. The relative independence of the information contained in measurements of phase velocity and ellipticity can be studied by investigating the linear independence of vectors whose components are empirically determined partial derivatives of phase velocity and ellipticity with respect to layer parameters. Such a study indicated that the information contained in the two measurements in the period range of interest (15-50 seconds) is largely independent. Thus a study combining both phase velocity and ellipticity should lead to a more realistic crustal structure than could be obtained by measurements of only one quantity.

Such a study was performed for the northern segment of the LASA in Eastern Montana. Refraction measurements made by the U.S. Geological Survey (Borchordt an' Roller, 1967) give the thicknesses and compressional velocities in the (assumed) layered crust; near surface geologic studies using petroleum company drill holes give the sedimentary thicknesses and velocities. Densities were obtained by using published empirical velocity-density relationships (e.g., Birch, 1964). Shear velocities in the layers were varied until a reasonable fit of both measured ellipticity and phase velocity was obtained. Two models satisfying the above

constraints are given in Table 1. Measured ellipticity (from one site) and phase velocity are compared with theoretical values in figures 1 and 2. A unique model can obviously not be found, but within the limitations of the assumptions of perfect elasticity and horizontally plane layered structure and the constraints imposed by other geophysical measurements the models listed are more realistic than any other models tried.

References:

Birch, Francis (1964). Density and composition of mantle and core, JGR, 69, 4377-4388.

Borcherdt, C.A., and J.C. Roller (1967). Preliminary Interpretation of a Seismic-Refraction Profile Across the Large Aperture Array, Montana, Tech. Letter 2, National Center for Earthquake Research.

Haskell, N.A. (1964). Radiation pattern of surface waves from point sources in a multilayered medium, BSSA, 54, 377-393.

MODEL LA65

Thickness (KM)	Compressional Velocity (KM/SEC)	Shear Velocity (KM/SEC)	Density (G/CM^3)
.67	2.1	1.4	2.0
.68	2.6	1.7	2.2
.40	4.0	2.5	2.4
.79	5.6	3.6	2.7
16.4	6.1	3.7	2.8
27.5	6.7	3.8	3.0
20.0	8.3	4.6	3.5
∞	8.3	4.8	3.5

MODEL LA66

Thickness (KM)	Compressional Velocity (KM/SEC)	Shear Velocity (KM/SEC)	Density (G/CM^3)
.67	2.1	1.4	2.0
.68	2.6	1.7	2.2
.40	4.0	2.5	2.4
.79	5.6	3.6	2.7
16.4	6.1	3.6	2.8
27.5	6.7	3.8	3.0
20.0	8.3	4.6	3.5
∞	8.3	4.8	3.5

TABLE I. Derived LASA crustal models
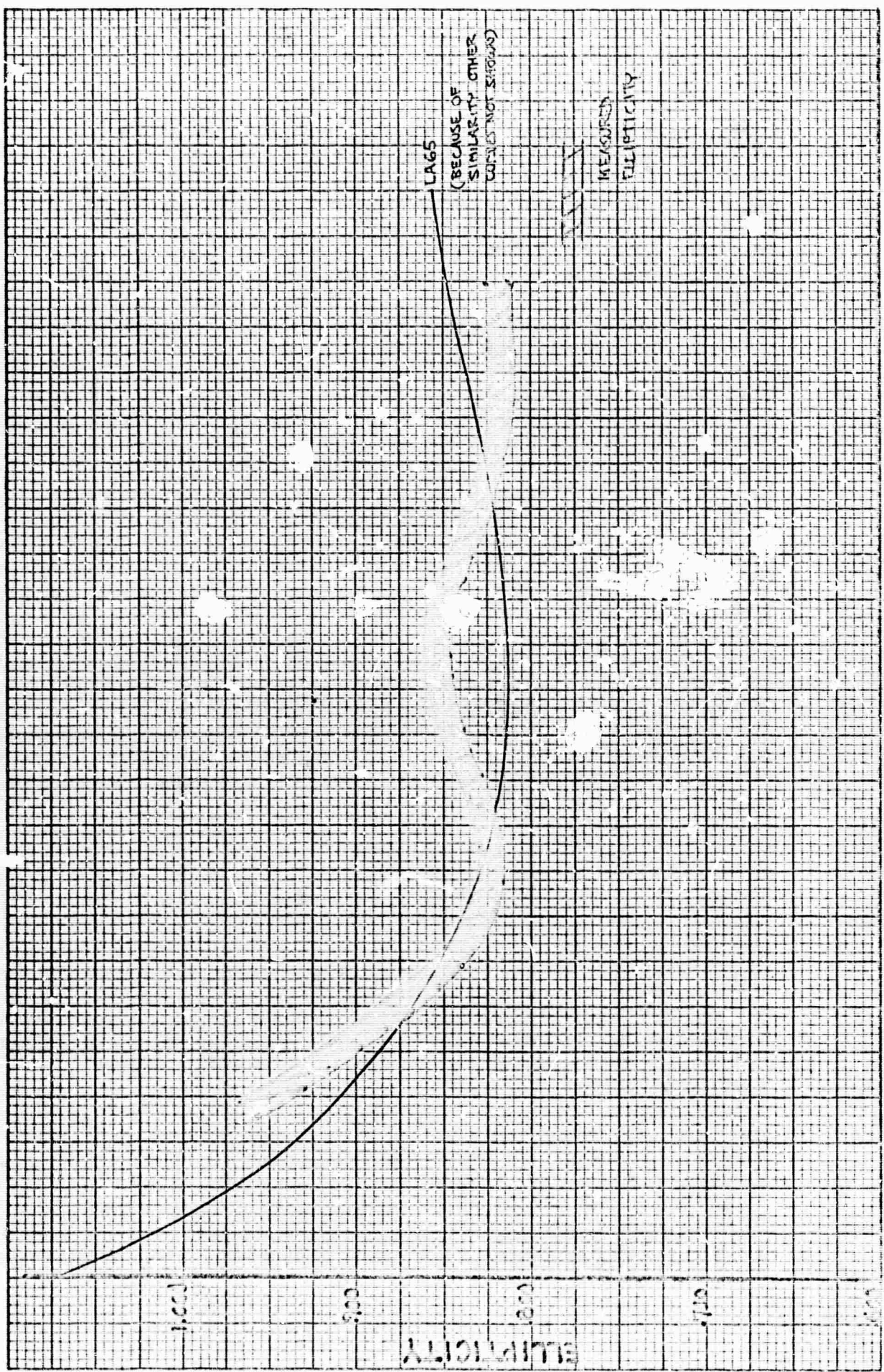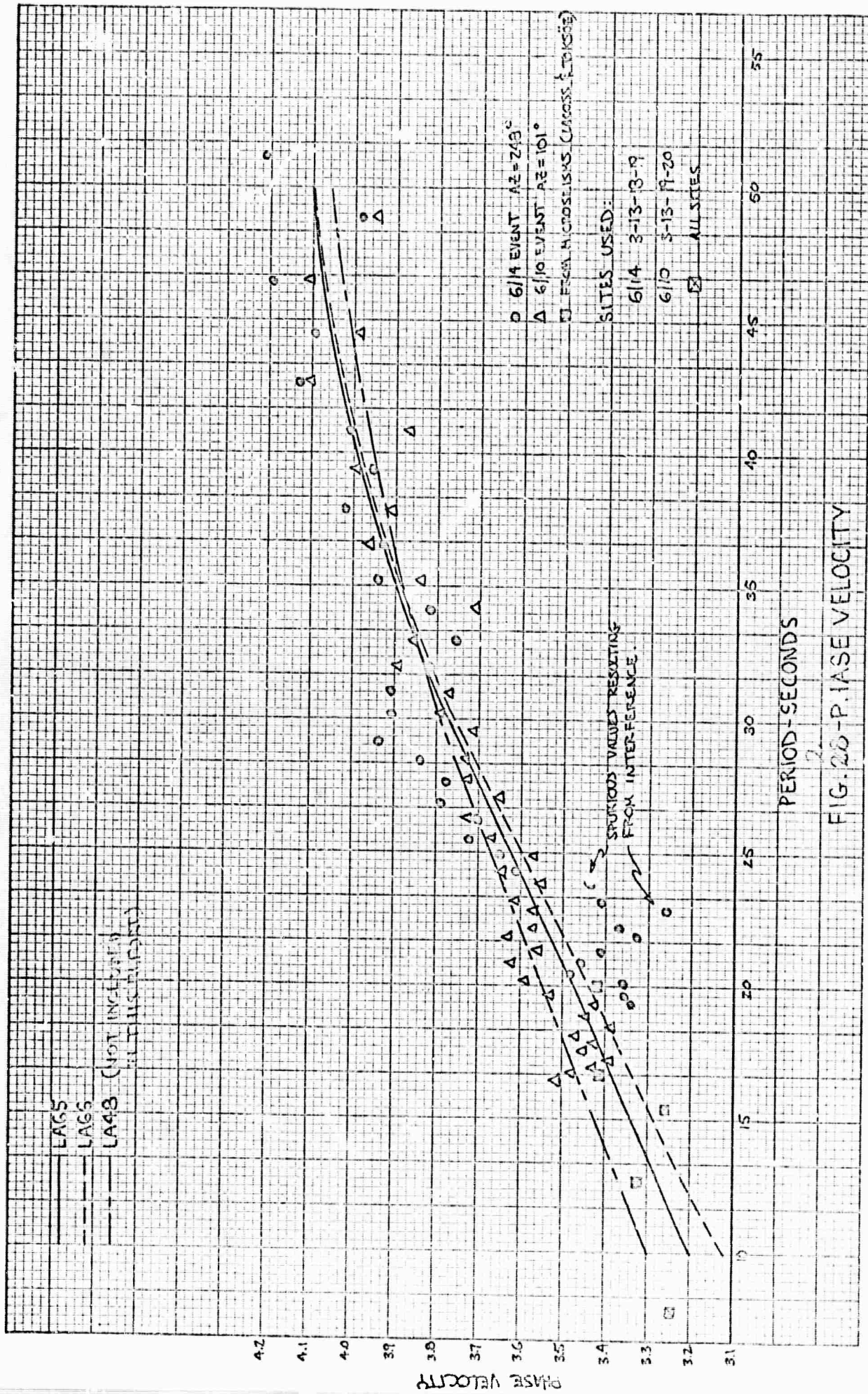
Fig 1

FIG. 28 - PHASE VELOCITY

III STRUCTURE AND INHOMOGENEITIES OF THE UPPER MANTLE

III. 1. Soft Layers in the Upper Mantle Under Japan

For revealing fine details of the crust-mantle structure, it is important to combine data from many independent sources. The refraction, Rayleigh wave and gravity methods have been most commonly used for this purpose. It has been noted that the couplings between any two of these methods are rather loose, because each of them is primarily controlled by an independent layer parameter; namely, compressional velocity, shear velocity or density.

A stronger coupling may be expected for combined use of Love, Rayleigh and S waves, because they are controlled by a common parameter, shear velocity. When we combine these data for Japan, we find that any weakly heterogeneous isotropic model cannot explain the observations.

Love wave velocities in Japan are lower by about 0.1 km/sec than those in the Canadian Shield. S wave velocities measured by the use of earthquakes occurring in the mantle within the network of Japan Meteorological Agency are consistent with Love wave velocities. On the other hand, Rayleigh wave velocities in Japan are about 0.3 km/sec lower than those in the Canadian Shield. This striking difference may be explained by a strongly heterogeneous model. It was found that if soft thin layers are interleaved in the upper mantle, Rayleigh wave velocities drop drastically while Love wave velocities are reduced only by a small amount.

Dispersion curves of Rayleigh and Love waves are computed for several laminated models, as shown in Figure 1. Case 2, which

includes 2% soft layers with shear velocity as low as 1.1 km/sec, explains observed velocities of both Rayleigh and Love waves.

If these soft layers represent the channels and reservoirs of magma, their shapes make an interesting contrast to those under the mid-ocean ridges, where the magma sheets are generally believed to be vertical.

Reference:

K. Aki, Seismological evidences for the existence of soft thin layers in the upper-mantle under Japan, J. Geophys. Res., (in press), 1967.

Figure showing phase velocity in km/sec versus period in sec for Love and Rayleigh waves, comparing unlaminated and laminated (1), (2), (3) models with data points for + Canadian Shield, ○ Central Japan, ⊙ Average Japan.
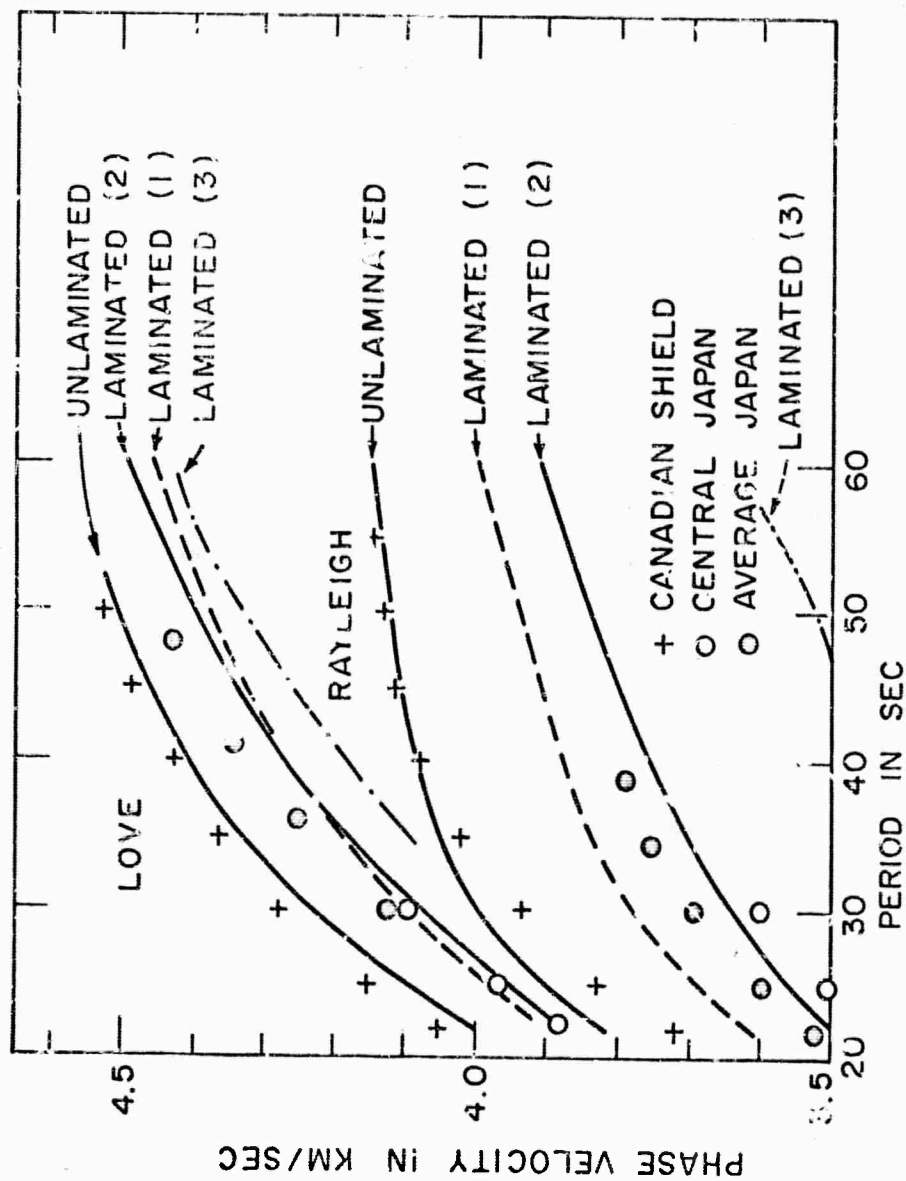
III.2. · Analysis and Correlation of Geophysical Data

In recent years increasing numbers of geophysical measurements have become available on a global basis. These provide an excellent means for the joint interpretation of various geophysical phenomena in terms of the properties of the earth's crust and mantle. The purpose of this paper is to collect and analyze these data and reduce them to a uniform format suitable for joint interpretation. The phenomena we consider are: gravitational potential, surface heat flow, surface topography, crustal thickness, seismic velocities (P_n) at Mohorovicic discontinuity, travel time residuals, and the non-dipole component of the earth's magnetic field. Since all data are not distributed at common locations, we cannot make a direct comparison, and we represent the measurements in terms of spherical harmonics and correlate the coefficients.

We use data from all available sources. The variations of the earth's gravitational potential have been studied from the orbits of the artificial satellites (Izsak, 1963; Guier and Newton, 1965; Kaula, 1963, 1966). The coefficients of the spherical harmonics, representing the geopotential variations at the surface of the earth, are determined through 8th order of harmonics. Heat flow values at the surface of the earth have been tabulated and analyzed and the coefficients are available through third order (Lee and MacDonald, 1963; Lee and Uyeda, 1965). Similarly, spherical harmonic coefficients of surface topography of the earth (Lee and Kaula, 1967), and the secular variation of the non-dipole part of the geomagnetic field (Cain, et al., 1965) are also available.

Deviation of the travel times of seismic waves from the Jeffreys-Bullen tables at some distance ranges have been well

known (Herrin and Taggart, 1966; Carder, et al., 1966; Cleary and Hales, 1966; Hales and Doyle, 1967; Chinnery and Toksöz, 1967; Toksöz, et al., 1967). In addition to these variations, different seismic stations show well defined residuals regardless of the epicentral distance. These station residuals which can be as much as ± 1.5 seconds must be due to structure of the crust and the mantle under the station. These residuals were discussed and analyzed in an earlier paper (Toksöz and Arkani-Hamed, 1967).

The crustal data are important, since the crust of the earth affects all the surface measurements thus obscuring the effects due to the variations in the properties of the earth's mantle. To determine the extent of this crustal biasing, and to study the possibility of its elimination, we have collected and analyzed the available crustal velocities and the P wave velocity below the crust (P_n). The analysis technique is described in the following section of this paper. The correlation of crustal and all other data are described in section 3.

Spherical Harmonic Analysis of Crustal and Seismic Data

In this section, we briefly describe the representation of crustal data in terms of spherical harmonics. Such an analysis is necessary for comparison of sets of data which are not distributed at overlapping locations.

The crustal data consists of crustal thickness, and P wave velocities in crustal layers and the P_n velocity at the top of the mantle. These are listed in Table I. The sources are numerous and include the results of seismic refraction, reflection, and surface wave dispersion measurements.

At each station the average crustal velocity is calculated using

$$V_j = \sum_{i=1}^{N_j} H_{ij} \Big/ \sum_{i=1}^{N_j} (H_{ij}/v_{ij}) \tag{1}$$

where H_{ij} and v_{ij} are thickness and compressional velocity, respectively, in layer i, and N_j is the total number of layers. In all cases the station elevations are reduced to sea level before calculation of average velocities. In Table II, the list of stations, their elevation, crustal thickness, P_n, and the average crustal velocities are tabulated.

In addition to the crustal data, we have also reanalyzed the deviation of seismic travel times at a large number of stations from average travel times. The data for these travel-time residuals are taken from tables of Herrin and

Taggart (1966), and they are discussed in detail in an earlier paper (Toksöz and Arkani-Hamed, 1967).

To minimize biasing, due to uneven distribution and varying density of stations, we average the data over a grid of 5° x 5° latitude and longitude. The global distributions of the averaged crustal thicknesses and P_n velocities is shown in Figure 1. The distribution of the travel time residuals is shown in Figure 2.

The averaged data are expressed in terms of spherical harmonics as

$$ Z = \sum_{n=0}^{3} \sum_{m=0}^{n} \left(A_{nm} \cos m\varphi + B_{nm} \sin m\varphi \right) P_{nm}(\cos\theta) \qquad (2) $$

where A_{nm} and B_{nm} are coefficients to be determined. Since we are primarily interested in variations, we first remove the mean value of each set of data. These correspond to zero order coefficients. Coefficients of non-zero order are determined using two different techniques. For crustal thickness and P_n velocities, where spatial distribution of data is fairly uniform, the simple least-squares method is used. The seismic travel time residuals are available mainly on the continents and land masses, and thus, have a very non-uniform distribution. In this case, a weighted least-square procedure is adopted. Both of these analysis techniques are described in Appendix I.

The harmonic coefficients through third order and degree (m,n = 0,3) are listed in Table III. In addition to crustal and seismic travel time residuals, we have included the coefficients for other data (heat flow, surface topography, geoid heights, secular variation of geomagnetic field) for easy reference.

In the analysis of the crustal data and travel time residuals, we have also computed the standard deviations of the coefficients. These were done by introducing artificial sets of random data. The procedure is discussed in detail in Appendix I.

The contoured surface variations of the crustal data and seismic travel time residuals are shown in Figures 3-5. These plots are based on the computed coefficients listed in Table III. In spite of the low order harmonics, travel time residuals essentially delineate the ocean basins, shield areas and tectonic regions. However, for a good fit, the crustal thicknesses appear to require coefficients of higher order than those computed in this paper. Unfortunately the density of the available data points would not justify the computation of still higher order coefficients.

Correlation of Geophysical Data

To determine the existence and/or lack of linear relationship between the various sets of geophysical data listed in this paper, we compute the correlation coefficients between any two sets. If different sets of data had common locations we could compute correlation coefficients using the sets of raw data and the definition

$$\rho_{xy} = \frac{\overline{(x-\bar{x})(y-\bar{y})}}{\sigma_x \cdot \sigma_y} \tag{3}$$

where $\bar{\xi}$ is the mean value of ξ and σ_ξ is the standard deviation of ξ.

In the cases where data do not have common spatial distribution, the spherical harmonic coefficients can be used to compute the correlation. If A_{nm}, B_{nm} and C_{nm}, D_{nm} are the spherical harmonic coefficients of the two phenomena their correlation coefficient can be expressed, using the orthogonality properties, as

$$\rho = \frac{\sum\limits_{n=0}^{N} \sum\limits_{m=0}^{n} \left(A_{nm} \cdot C_{nm} + B_{nm} \cdot S_{nm} \right)}{\left[\sum\limits_{n=0}^{N} \sum\limits_{m=0}^{n} \left(A_{nm}^2 + B_{nm}^2 \right) \right]^{1/2} \cdot \left[\sum\limits_{n=0}^{N} \sum\limits_{m=0}^{n} \left(C_{nm}^2 + S_{nm}^2 \right) \right]^{1/2}} \tag{4}$$

Using equation 4 and the coefficients listed in Table III, we computed the correlation coefficients between crustal and other geophysical data. The correlation matrix is given in Table IV. The accuracy limits of these coefficients are not shown in the table. These will be discussed in the next section.

Discussion

The correlation coefficients given in Table (4) summarize
the results of our analysis. Before discussing these coeffi-
cients, we should mention that they are based on the spherical
harmonic coefficients. Thus, the coefficients represent cor-
relations between broad variations. The problem is somewhat
more complicated because of the aliasing effect and the
accuracy of the coefficients. First of all, some of the
data that are analyzed (heat flow, travel time residuals,
crustal parameters) are sparsely distributed and we cannot
justify harmonics higher than three. These low harmonics
are probably biased by the higher order variations that may
be affecting the data. This biasing is examined in the case
of travel time residuals, by generating artificial data and
re-expanding it in terms of spherical harmonics and comparing
the results. In other words, we generated artificial data
at the same points where we have real data, using spherical
harmonics, including all harmonics from zero to n, and adopt-
ing unity for the coefficient of each harmonic. Then we
expanded the obtained data in terms of spherical harmonics
up to and including the third harmonic and compared the
corresponding coefficients. We followed this process for
8 values of n, (n = 2,3,. . .,9). The corresponding coeffi-
cients do not in general differ by more than 30% for the
values of n up to 6. Including values 7, 8, or 9 of n
changes the coefficients significantly. This shows that,
due to the location of the stations, the harmonics of the
order higher than 7 contribute to the low harmonics
(n = 0,. . .,3).

We have, also, estimated the accuracy of the coefficients of the crustal parameters by introducing artificial sets of random data to obtain uniform coverage over the earth. The standard deviations computed by this method are shown in Table III. They range in value from a few percent to more than hundred percent of the absolute value of the coefficients. In general, the coefficients with small magnitudes are least reliable. Those with relatively high magnitudes are reliable to better than ±20 percent.

The correlation coefficients listed in Table (4) are in general low except for a few cases. Highest correlation is between surface topography and crustal thicknesses This means that higher regions are associated with a thicker crust, an obvious conclusion when we consider the oceans and the continents and the associated crustal thicknesses. Heat flow values and travel time residuals are also correlated with topography. For the former, the correlation coefficient is positive indicating a higher heat flow for topographically higher regions. This is reasonable when we consider the relatively high heat flow on tectonic regions and low heat flow in abyssal plains of the ocean. The negative correlation between travel time residuals and topography or crustal thickness is somewhat surprising. This means that oceanic areas are relatively slow and continents are fast, which implies that the upper mantle velocities under the oceans are slower than those under the continents to offset the crustal delays. We must consider one point, however, that our seismic travel time data are sparse in the oceans and those which are available come from the islands. These may be anomalous points giving

a false representation of the oceanic regions.

The correlation of travel time residuals with both heat flow and geopotential is poor. In both cases, the correlation coefficients are negative indicating low seismic velocities corresponding to low densities and to high heat flow or temperature.

The lack of correlation between geopotential and surface topography, crustal thickness, or P_n velocity is very significant. These results which have also been observed by Kaula (1968) indicate that lower harmonics of geopotential variations are controlled by mass distributions in the mantle, which also agree with McKenzie's (1967) conclusion.

Another significant correlation coefficient is between the secular variations of geomagnetic field and geopotential. One explanation could be the irregularities of the core-mantle boundary as discussed by Hide (1967) leading to strong density anomalies and affecting the magnetic field of the earth.

The reliability of the correlation coefficients is an important question. Using the upper and lower limits of the harmonic coefficients we have computed the variations of the correlation coefficients. In general, these variations are less than $\pm$ 0.1. With the availability of more data and improved analysis techniques, in the future, we expect to improve the accuracy of the spherical harmonic coefficients and, hence, the correlation matrix listed in Table (4).

In conclusion, we can state that the low order harmonics of the gravitational field of the earth are due to an anomalous density distribution in the mantle. Moreover, there is a significant lateral variation of the velocity of seismic waves in the upper mantle which overcomes the crustal effects.

Appendix

In this appendix we describe the spherical harmonic analysis techniques we have used for the analysis of the discrete geophysical data.

Let $D(\theta_i, \varphi_i)$, $i = 1, \cdots, q$ be the observed values to be expressed in terms of the spherical harmonics.

$$Z(\theta, \varphi) = \sum_{n=0}^{14} \sum_{m=0}^{n} (A_{nm} \cos m\varphi_i + B_{nm} \sin m\varphi_i) P_{nm}(\cos\theta_i) \qquad (1)$$

where θ_i = co-latitude, φ_i = east longitude

$P_{nm}(\cos\theta_i)$ =fully normalized associated Legendre polynomial. To determine the coefficients A_{nm}, B_{nm} we have used two slightly different procedures.

a) Least-squares method.

This method requires the minimizing of the squared error, E^2, in determining the coefficients. The error is defined by

$$(2) \qquad E^2 = \sum_{i=1}^{q} \left[Z(\theta_i, \varphi_i) - D(\theta_i, \varphi_i) \right]^2$$

where Z is the calculated value and D is the value of the data at θ_i, φ_i. The minimization requires

$$(3) \qquad \frac{\partial E^2}{\partial A_{k\ell}} = \frac{\partial E^2}{\partial B_{k\ell}} = 0.$$

The combination of equations (1), (2), and (3) leads to

$$(4) \qquad \overline{\overline{S}} \cdot \vec{X} = \vec{R}$$

where $\overline{\overline{S}}$ is a symmetric matrix, any element of which is a two by two matrix,

$$(5) \qquad S_{k\ell, nm} = \begin{bmatrix} \sum_{i=1}^{q} \cos m\varphi_i \cos \ell\varphi_i \, P_{nm} P_{k\ell} & \sum_{i=1}^{q} \sin m\varphi_i \cos \ell\varphi_i \, P_{nm} P_{k\ell} \\ \sum_{i=1}^{q} \cos m\varphi_i \sin \ell\varphi_i \, P_{nm} P_{k\ell} & \sum_{i=1}^{q} \sin m\varphi_i \sin \ell\varphi_i \, P_{nm} P_{k\ell} \end{bmatrix}$$

and $\vec{X}$ and $\vec{R}$ are column vectors

(6)
$$X_{nm} = \begin{bmatrix} A_{nm} \\ B_{nm} \end{bmatrix} \quad , \quad K_{k\ell} = \begin{bmatrix} \sum_{i=1}^{q} D(\theta_i, \varphi_i) \cos k\varphi_i \, P_{k\ell} \\ \sum_{i=1}^{q} D(\theta_i, \varphi_i) \sin k\varphi_i \, P_{k\ell} \end{bmatrix}$$

If there were infinite numbers of evenly distributed
data points, the orthogonality properties of the spherical
harmonics could be used in solving equation (4) for $\bar{\bar{X}}$.
In practice, however, there are finite numbers of unevenly
distributed data points, and we can use the Gauss-Jordan
reduction technique (Hildebrand, 1961).

b) Weighted least-squares method.

As mentioned above the limited and uneven distribution
of data makes it difficult to satisfy the orthogonality proper-
ties of the spherical harmonic directly. Thus each harmonic
obtained may have a contibution from other harmonics. To mini-
mize this probelm we find a weighting factor, ω , for each
data point such that the harmonics are orthogonal on the
weighted points. That is

$$\sum_{i=1}^{q} \omega_i \, y_{k\ell}(\theta_i, \varphi_i) \cdot y_{nm}(\theta_i, \varphi_i) = \delta_{mk} \cdot \delta_{\ell n} \cdot \sum_{i=1}^{q} \sin \theta_i \, y_{k\ell}^2(\theta_i, \varphi_i) \quad (7)$$

where $y_{k\ell}(\theta, \varphi)$ is the spherical harmonic of order k and degree ℓ
$\left(y_{k\ell}(\theta, \varphi) = (\cos, \sin) k\varphi \cdot P_{k\ell}(\cos \theta) \right)$, and δ_{kn} is the kroni-
ker delta function. We make the factors as closely represen-
tative of the areas as possible by minimizing η^2, where η^2
is defined by

$$\eta^2 = \sum_{i=1}^{q} \left(\omega_i - \sin \theta_i \right) \quad (8)$$

ω_i is the weighting factor of the ith data point and θ_i
is its co-latitude. In computation we first solve equations
(7) and (8) for ω_i's . Rewriting (7) and (8) in a compact
form, we obtain

$$\bar{\bar{F}} \cdot \bar{\omega} = \bar{B} \quad (9)$$

$$\left(\bar{\omega} - \bar{s} \right)^T \cdot \left(\bar{\omega} - \bar{s} \right) = Min. \quad (10)$$

where $\bar{\bar{F}}$ is a pxg matrix $\left(p = \frac{(n+1)(n+2)}{2} \cdot \{(n+1)(n+2) + 1\} \right)$,

N is the highest order of the harmonics included.

$$\bar{F}_{n,m,k\ell}(\theta_i, \varphi_i) = Y_{nm}(\theta_i, \varphi_i) \cdot Y_{k\ell}(\theta_i, \varphi_i) \qquad (11)$$

and $\bar{W}$, $\bar{\xi}$, and $\bar{B}$ are column vectors with q, q and P rows respectively.

$$w_i = w_i \; , \quad \xi_i = z_i \, c_i \qquad B_{nm,k\ell} = \delta \cdot \delta \sum_{i=1}^{q} w_i \, z_i \, Y_{k\ell}(\theta_i, \varphi_i) \qquad (12)$$

Equations (9) and (10) can be solved approximately by minimizing I where I is defined by

$$I = (\bar{\bar{F}} \cdot \bar{W} - \bar{B})^T \cdot (\bar{\bar{F}} \cdot \bar{W} - \bar{B}) + \varepsilon \, (\bar{W} - \bar{\xi})^T \cdot (\bar{W} - \bar{\xi}) \qquad (13)$$

The weighting factors are determined from

$$\bar{W} = (\bar{\bar{F}}^T \cdot \bar{\bar{F}} + \varepsilon \, \bar{\bar{I}})^{-1} \cdot (\bar{\bar{F}}^T \bar{B} + \bar{\varepsilon}) \qquad (14)$$

spherical harmonic coefficients are determined by minimizing the weighted least squares,

$$\sum_{i=1}^{q} w_i \left\{ Z(\theta_i, \varphi_i) - Z'(\theta_i, \varphi_i) \right\}^2 = Min. \qquad (15)$$

and A_{nm} and B_{nm} are given by

$$\begin{bmatrix} A_{nm} \\ B_{nm} \end{bmatrix} = \sum_{i=1}^{q} w_i \, Z(\theta_i, \varphi_i) \cdot \begin{bmatrix} \cos m\varphi_i \\ \sin m\varphi_i \end{bmatrix} \cdot P_{nm}(\cos\theta_i) \qquad (16)$$

Variance of Coefficients

The accuracy of the analysis depends strongly on the number of data points and their distribution. One way of

determining the accu.acy of the coefficients and the effect
of new data points is to determine the variance of the coeffi-
cients. For this let us generate randomly a set of artificial
data on the $5°$ x $5°$ squares where there are no real data. These
new data should have the following properties: (1) The mean
of the random values at a point is equal to the spatial mean
of the available data, (2) the variance of the random values
at a point is equal to the spatial variance of the real data.

In actual computation we generate the random data with
the above properties to cover all the $5°$ x $5°$ squares of the
earth's surface which do not have real observed data. Then,
we expand the data obtained, re 1 and artificial, in terms of
the spherical harmonics. Because of the large number of
evenly distributed data, the harmonics are nearly orthogonal
and the coefficients of the harmonics can be determined using

$$
C_{nm} = K_{nm} \left\{ \sum_{i=1}^{q} d(i) y_{nm}(i) \sin\theta_i + \sum_{j=1}^{L} s(j) y_{nm}(j) \sin\theta_j \right\} \tag{17}
$$

In (17) d is the real data and s is the artificial random data,
q is the number of squares with real data and L that of the
artificial data. $K_{nm} = 1/\sum_{i=1}^{M} y_{nm}^2(i)\sin\theta_i$, and C_{nm} represents
either A_{nm} or B_{nm}. M is the number of squares on the earth's
surface.

The variance of C_{nm} is defined by

$$
\sigma^2_{C_{nm}} = \frac{1}{T} \cdot \sum_{t=1}^{T} \left\{ C_{nm}(t) - \frac{1}{T} \sum_{i=1}^{T} C_{nm}(i) \right\}^2 \tag{18}
$$

where T is the number of random functions adapted. Using

the preceding assumptions and equation (17), we obtain

$$\sigma^2_{C_{nm}} = K_{nm} \cdot \sigma^2_d \cdot \sum_{J=1}^{L} y^2_{nm}(j) \sin^2 \theta_j \qquad (19)$$

where σ^2_d is the variance of the real data.

Acknowledgements

REFERENCES

Cain, J. C., W. E. Daniels, Shirley J. Hendricks, and Duane C. Jensen, An evaluation of the main geomagnetic field, 1940-1962, J. Geophys. Res., 70, 3647-3674, 1965.

Carder, D. S., D. W. Gordon, and J. N. Jordan, Analysis of surface-foci travel times, Bull. Seis. Soc. Am., 56, 815-840, 1966.

Chinnery, M. A. and M. N. Toksöz, P-wave velocities in the mantle below 700 km., Bull. Seis. Soc. Am., 57, 199-226, 1967.

Cleary, J. and A.L. Hales, An analysis of the travel times of P-waves to North American stations, in the distance range of 32^0 to 100^0, Bull. Seism. Soc. Am., 56, 467-489, 1966.

Guier, W. H. and R.R. Newton, The earth's gravity field as deduced from the doppler tracking of five satellites, J. Geophys. Res., 70, 4613-4626, 1965.

Hales, A.L. and H. A. Doyle, p and s travel time anomalies and their interpretations, Scientific report no. 4, AF 19 (628)-2936, Southwest Center for Advanced Studies, 1967.

Herrin, E.T. and J. Taggart, personal communication , 1966.

Hide, R., Motions of the earth's core and mantle, and variations of the main geomagnetic field, Science, 157, 55-56, 1967.

Hildebrand, F. B., Methods of Applied Mathematics, page 1, 1961.

Izsak, I. M., Tesseral harmonics of the geopotential and corrections to station coordinates, J. Geophys. Res., 69, 2621-2630, 1964.

Kaula, W. M., Determination of the earth's gravitational field, Rev. of Geophys., 1, 507-551, 1963.

Kaula, W. M., Tesseral harmonic of the earth's gravitational field from camera tracking of satellites, J. Geophys. Res., 71, 4377-4388, 1966.

Kaula, W. M., Geophys. Space Science Reviews, 1968 (in press)

Lee, W.H.K. and W.M. Kaula, A spherical harmonic analysis of
    the earth's topography, J. Geophys. Res., 72, 753-758,
    1967.

Lee, W.H.K. and G.J.F. MacDonald, The global variation of
    terrestrial heat flow, J. Geophys. Res., 68, 6481-6492,
    1963.

Lee, W.H.K. and P.T. Taylor, Global analysis of seismic refrac-
    tion measurements, Geophys. J., R. Astr. Soc., 11, 389-
    413, 1966.

Lee, W.H.K. and S. Uyeda, Review of heat flow data, in Terres-
    trial Heat Flow, of Geophys. Monog. Ser., Am. Geophys.
    Union, 8, 87-190, 1965.

McKenzie, D.P., Some remarks on the heat flow and gravity
    anomalies, J. Geophys. Res., 72, 6261-6273, 1967.

Toksöz, M.N. and J. Arkani-Hamed, Seismic delay times: correla-
    tion with other data, Science, 158, 783-785, 1967.

Toksöz, M.N., M.A. Chinnery, and D. L. Anderson, Inhomogenei-
    ties in the earth's mantle, Geophys. J. R. Astr. Soc., 13,
    31-59, 1967.

List of Tables

NOTE: Tables 1 and 2 and the associated references are not included in this report.

Table 3(a)

n	m	Geopotential (x10⁻⁶ erg.)		Topography (Km)		Sec. var. of Geomagnetism (γ/year)		Heat flow (μ col/sec. cm²)	
		A_{nm}	B_{nm}	A_{nm}	B_{nm}	A_{nm}	B_{nm}	A_{nm}	B_{nm}
0	0				0.0			1.475	0.0
1	0			0.328	0.0			0.118	0.0
1	1			0.777	0.538			0.064	-0.018
2	0			0.339	0.0			-0.107	0.0
2	1			0.401	0.343			0.107	0.085
2	2	2.430	-1.390	-0.564	-0.140			-0.044	0.133
3	0	0.965	0.0	-0.110	0.0	-0.4	0.0	0.037	0.0
3	1	1.940	0.150	-0.078	0.158	-10.5	1.9	-0.162	-0.009
3	2	0.720	-0.780	-0.540	0.547	3.4	4.0	0.042	0.089
3	3	0.550	1.240	0.141	0.803	-1.9	-9.0	0.110	0.219
4	0	0.500	0.0			0.8	0.0		
4	1	-0.610	-0.490			5.4	-0.9		
4	2	0.330	0.710			-1.9	-1.7		
4	3	0.890	0.070			-0.2	3.2		
4	4	-0.310	0.110			0.8	-5.5		
5	0	0.050	0.0			3.5	0.0		
5	1	-0.050	0.030			-0.7	1.8		
5	2	0.750	-0.170			2.5	2.9		
5	3	-0.610	0.150			0.6	-0.8		
5	4					0.0	-0.4		
5	5					1.6	-0.2		

Table 3(b)

n	m	Crustal thickness (Km)		P_n velocity (Km/sec.)		Travel time residual (sec.)	
		A_{nm}	B_{nm}	A_{nm}	B_{nm}	A_{nm}	B_{nm}
0	0	18.963	0.0	8.070	0.0	0.248	0.0
1	0	2.522 ± .266	0.0	0.052 ± .004	0.0	-0.056 ± .011	0.0
1	1	1.355 ± .337	4.891 ± .323	-0.017 ± .004	-0.038 ± .005	-0.118 ± .014	-0.026 ± .014
2	0	5.836 ± .280	0.0	-0.066 ± .004	0.0	-0.028 ± .011	0.0
2	1	0.386 ± .302	3.073 ± .287	0.013 ± .005	0.003 ± .005	-0.146 ± .013	-0.042 ± .012
2	2	-0.487 ± .338	-1.217 ± .339	0.033 ± .005	0.033 ± .005	0.021 ± .014	0.084 ± .014
3	0	-0.842 ± .278	0.0	0.059 ± .004	0.0	-0.036 ± .012	0.0
3	1	1.096 ± .295	-8.030 ± .289	0.007 ± .005	0.030 ± .005	-0.034 ± .012	0.054 ± .012
3	2	-6.011 ± .310	2.534 ± .309	-0.027 ± .005	0.018 ± .005	0.088 ± .013	-0.006 ± .013
3	3	1.443 ± .340	1.772 ± .346	-0.050 ± .005	-0.033 ± .005	-0.045 ± .015	-0.088 ± .014

Table 4

	Geopotential	Topography	Sec. var.	Heat flow	Crustal thickness	P_n velocity	Travel time residual
Geo-potential	1.0	-0.23	-0.66	-0.21	-0.06	0.02	-0.33
Topography		1.0	---	0.49	0.74	-0.27	-0.73
Sec. var.			1.0	---	---	---	---
Heat flow				1.0	0.04	0.11	-0.34
Crustal thickness					1.0	-0.31	-0.58
P_n velocity						1.0	0.14
Trav. time resid.							1.0

Figure Captions

Figure 1.   Distribution of the crustal thickness and P_n
   velocity data averaged over 5° x 5° squares. Various
   symbols indicate different sources of data.

Figure 2.   Distribution of the seismic travel time resi-
   duals averaged over 5° x 5° squares.

Figure 3.   Contours of the seismic travel time residuals
   (in seconds) based on spherical harmonics of 3rd order.

Figure 4.   Contours of crustal thicknesses (in km) based
   on computed harmonics.

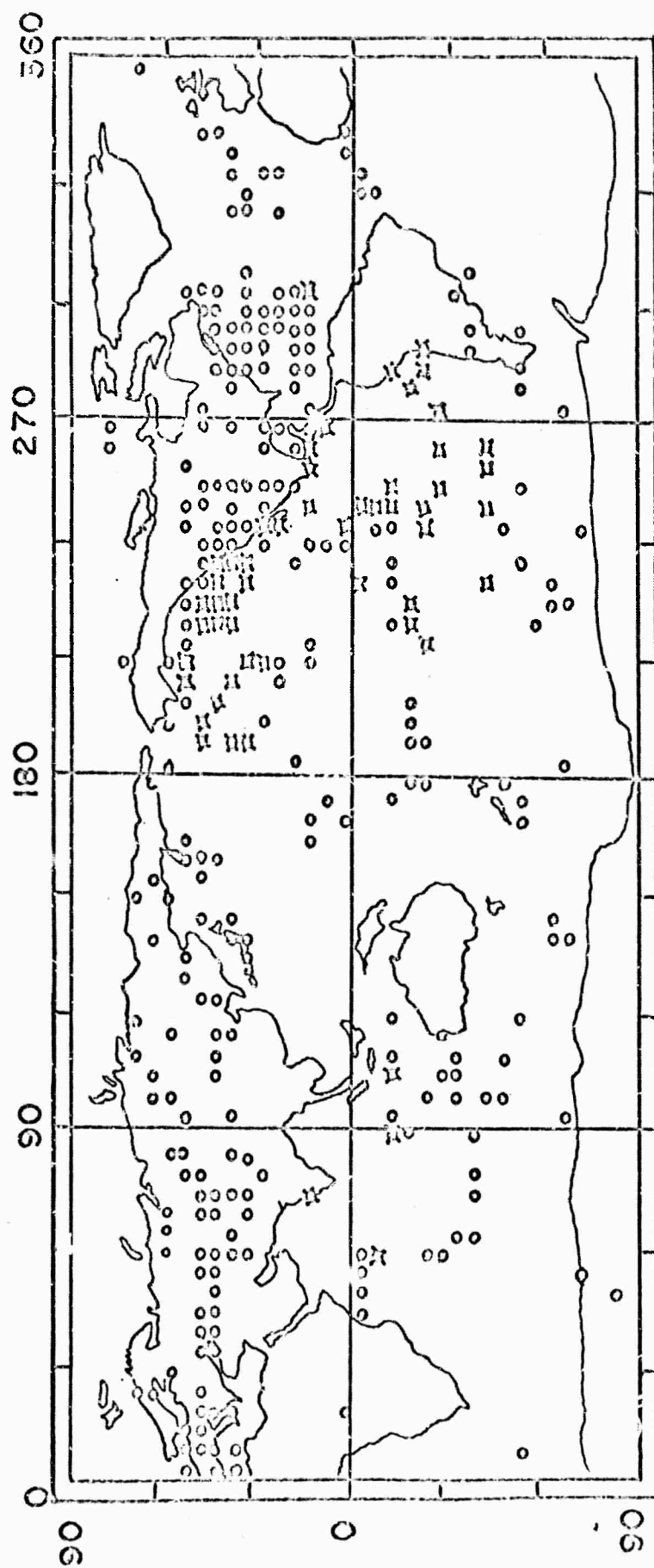Figure 5.   Contours of P_n velocities (km/sec) based on com-
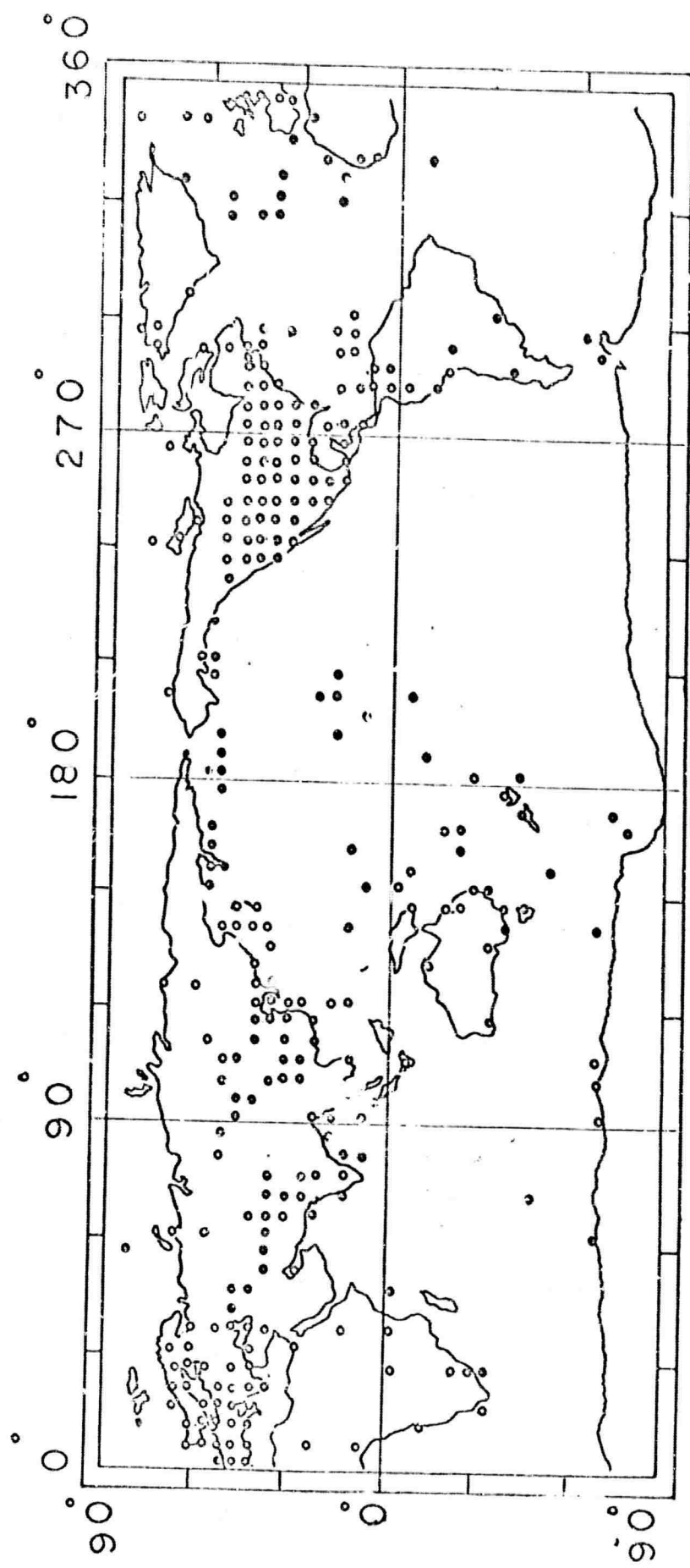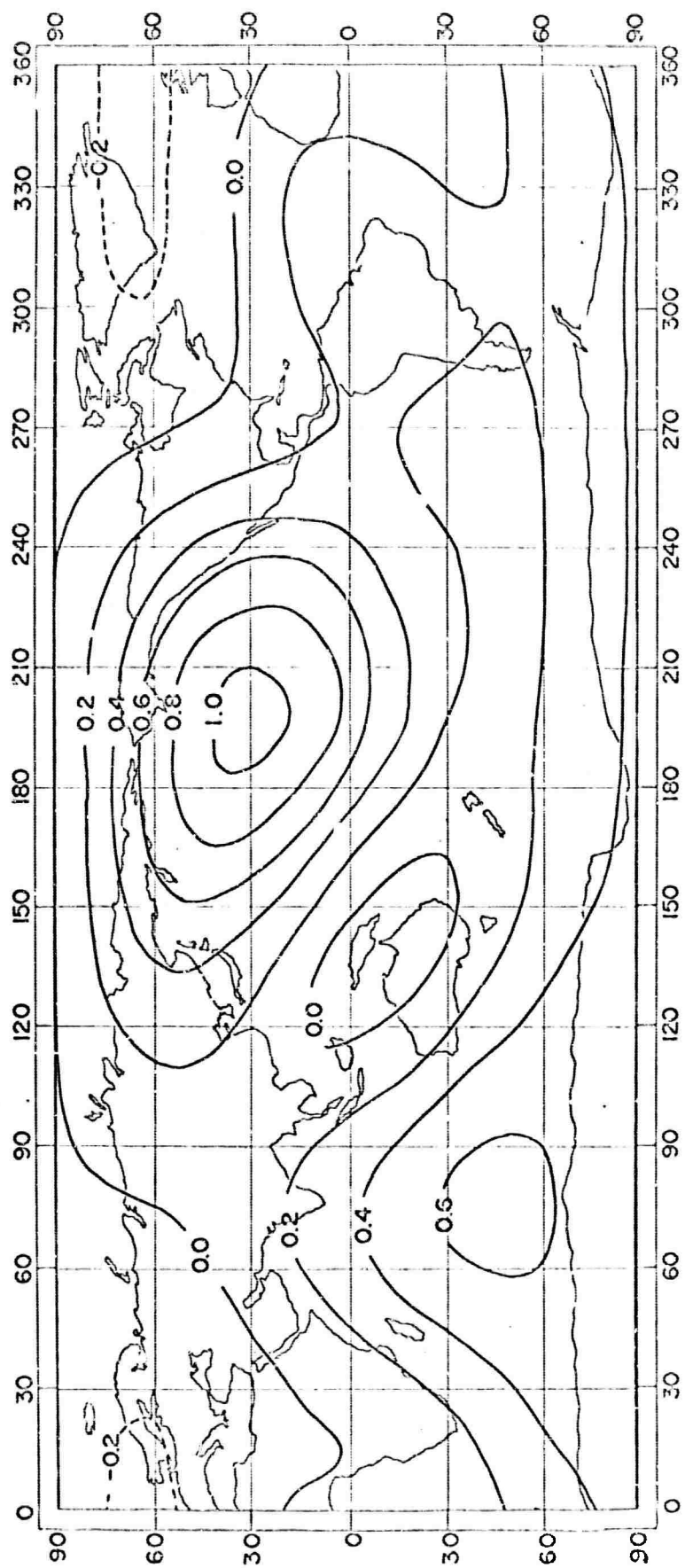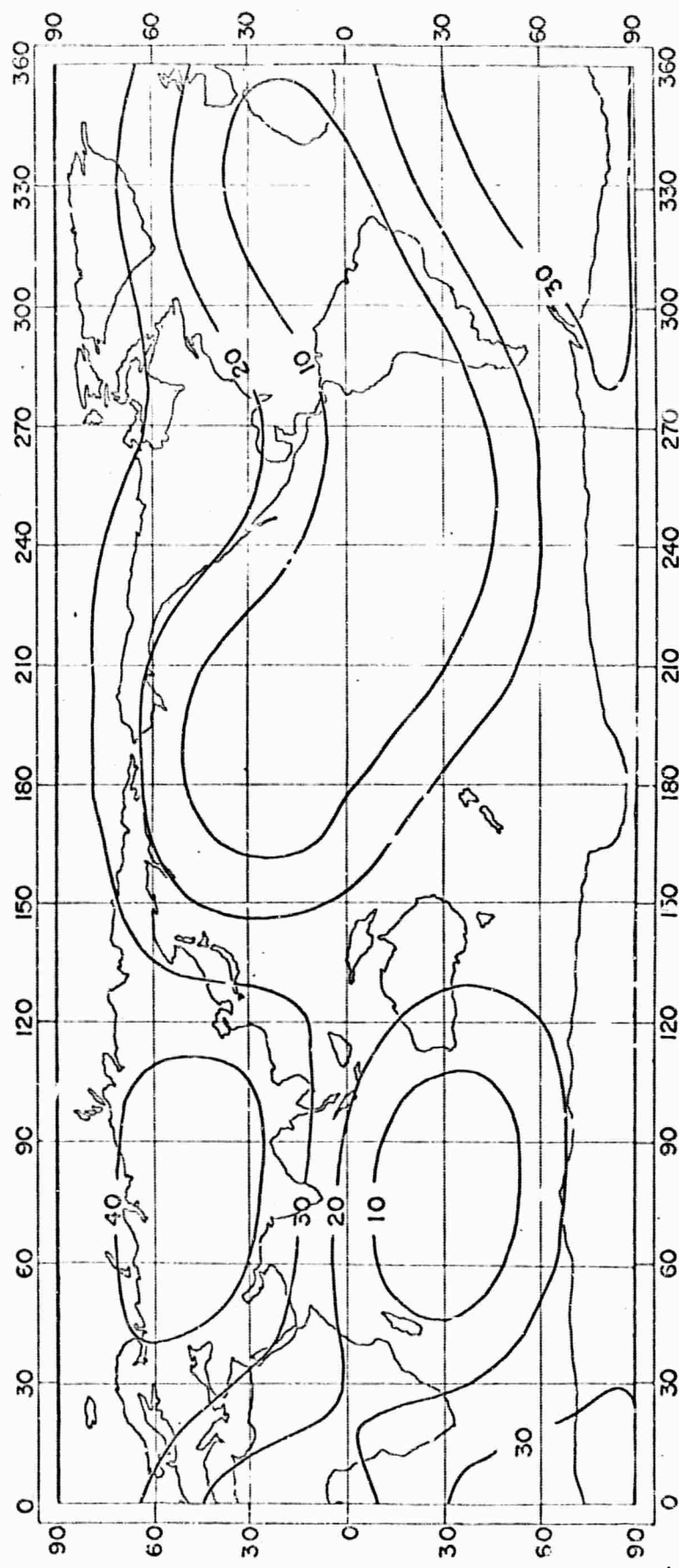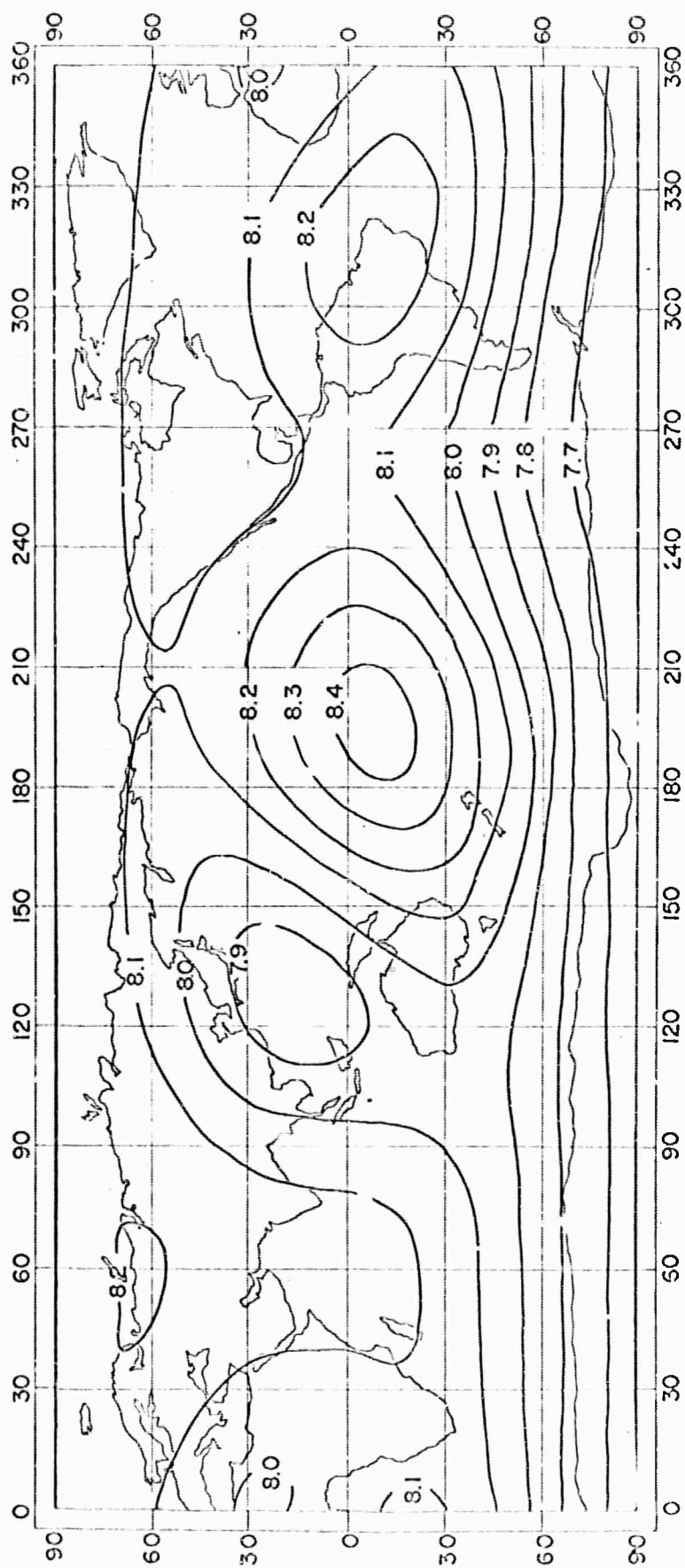   puted spherical harmonics.

Figure 1

Figure 2

Figure 4

Figure 5

IV SOURCE MECHANISM STUDIES AND PARKFIELD EARTHQUAKE

IV. 1. Seismic Displacements Near the Fault

The Parkfield earthquake of June 28, 1966 offers an
unusual opportunity for a detailed study of earthquake source
mechanism. For the first time in the history of seismology,
the ground movement was recorded practically at the fault, by
the strong motion accelerometer operated by the Coast and
Geodetic Survey.

An interesting feature of the record is that the displace-
ment perpendicular to the fault strike, obtained by twice-
integration of the accelerogram, shows an impulsive form with
1.5 sec duration and 30 cm height (Figure 2).

We have computed a theoretical seismogram based on a moving
dislocation model having parameters derived from near field
measurements. The synthesized seismogram (Figure 3) showed
a similar impulsive form, but the predicted pulse height was
smaller than the observed by an order of magnitude. The dis-
location must be about 60 cm, in order to explain the observed
movement, while the offset measured on the surface after the
earthquake was only 5 cm.

The above inconsistency may be resolved, if the superficial
layers were coupled from the deeper layers. The large dislocation
at depth is consistent with a geodimeter observation.

If we accept the evidence from the accelerometer, and combine the resultant dislocation with the seismic moment measured from surface waves, we must conclude that the fault depth is less than 5 km. This is 1/3 of the depth of the aftershock zone.

The value of stress drop was previously estimated at less than 1 bar, which is unusually low. This value must also be revised, if we accept the evidence from the accelerometers. The revised value is about 20 bars.

IV 2.   Analysis of Seismic Coda as Scattered Waves

A method was devised to extract information on earthquake source as well as on wave medium from the coda of local small earthquakes. The method is based on the assumption that the coda of local earthquakes consists of secondary waves generated by scatterers uniformly distributed in an area.

There are several evidences supporting this assumption; (1) the path effect on seismic spectra seems to disappear in the coda of local earthquakes (2) the total duration of seismogram for local earthquakes appears to be independent of epicentral distance, and (3) the spacial correlation of coda waves measured by seismometer arrays indicates that they are not unidirectionally propagating waves.

Using the data on the Parkfield aftershocks supplied from the Geological Survey, we found new evidences supporting the above assumption. (1) The coda spectrum is a function of only the time from the earthquake origin time, and independent of wave path and of source size. (2) Strong correlation exists between the coda intensity and local geology of the station site, suggesting that coda may be random standing waves formed by scattered waves coming from all directions. On the basis of the above assumption, we derived the transfer function of the scattering process from the coda of an earthquake with known seismic moment. The mechanism of scattering seems not of the Rayleigh type. The scatterer sizes appear to be greater than wave lengths involved.

The seismic moment was obtained for many micro-aftershocks of the Parkfield earthquake of June 28, 1966, from coda amplitudes by the use of the scattering transfer function. The relation between the seismic moment Mo and local magnitude M is determined as $\log M_O = 15.8 + 1.5M$ where the unit of M_O is dyne cm. The size of a micro-earthquake with magnitude zero is estimated as $10^m \times 10^m$.

References:

IV.1. Aki, K., Seismic displacements near the fault (in preparation), 1967.

Aki, K., Study of earthquake sources from the seismic spectrum, Publ. Dom. Obs., Ottawa, 1968, (in press).

IV.2. Aki, K., Analysis of seismic coda as scattered waves, J. Geophys. Res., 1968 (in press).

GAL
500

ACCELERATION

0

N 65°E

-500
CM/SEC
50

VELOCITY

0

N 65°E

-50
CM
10

DISPLACEMENT

0

-10

N65°E

-20

-30

5 SECONDS

-40
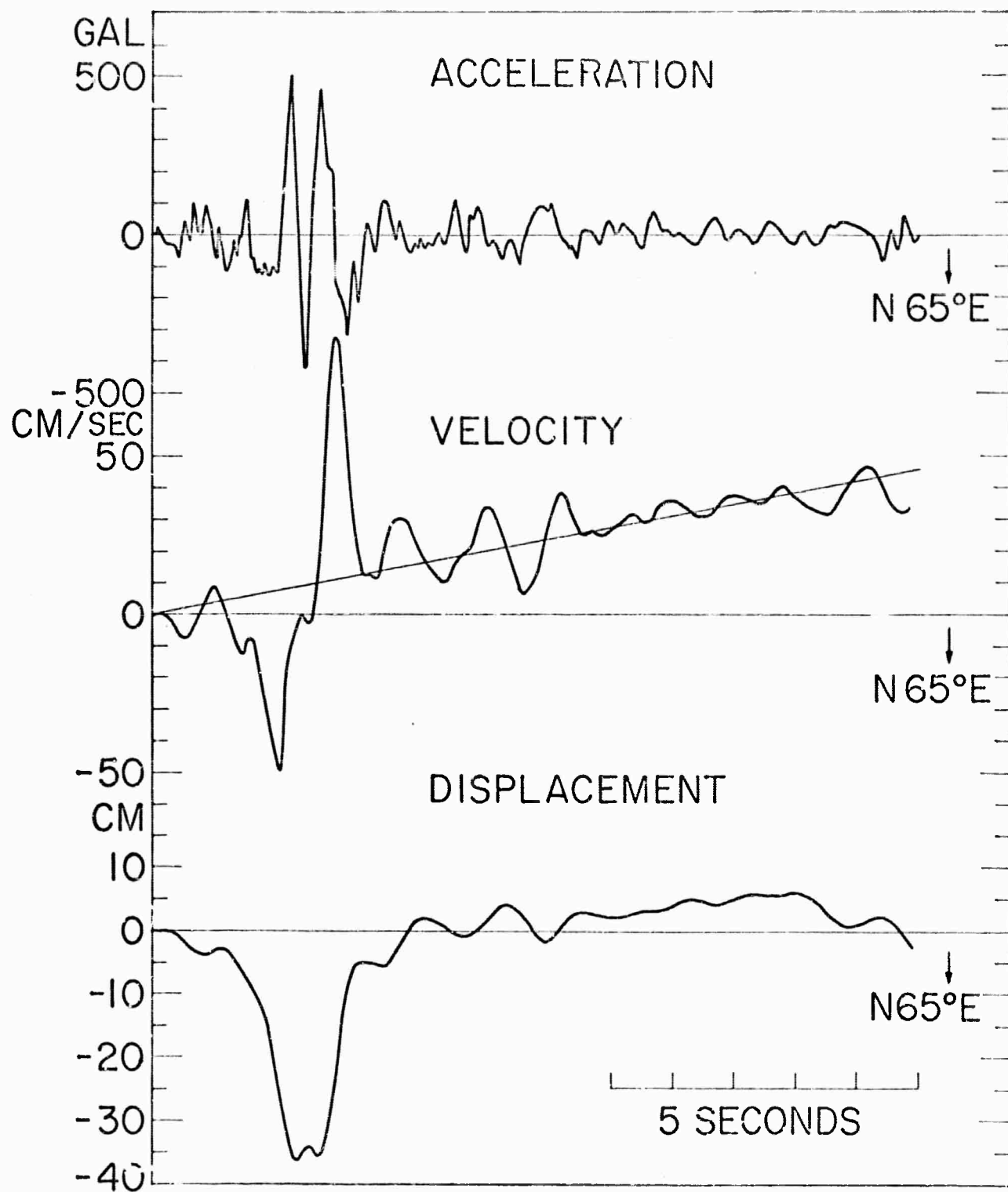
Fig. 2.

PARALLEL DISPLACEMENT

V = 2.2 km/sec

4 seconds

$0.66 \times D_0/2$

PERPENDICULAR DISPLACEMENT

V = 2.2 km/sec

$0.52 \times D_0$

PERPENDICULAR DISPLACEMENT

V = 3.4 km/sec

$0.72 \times D_0$

Fig. 3

IV.3.   Radiation and Dissipation of Love and Rayleigh Waves from
          the Parkfield Earthquake of June 28, 1966.

A comprehensive spectral analysis of Love and Rayleigh waves
was made for the Parkfield earthquake of June 28, 1966. Tentative
Q values were determined from records at two stations on a common
great circle path, for two paths; one entirely continental and
the other almost entirely oceanic. Assuming that these Q values
apply to all other continents and oceans, the observed spectra
were corrected for dissipation, and compared with the theoretical
spectra based on a dislocation source model having parameters
derived from various near field measurements. Figure 4 and Figure
5 show examples of such a comparison. Both Love and Rayleigh
wave spectra showed a consistent value of the seismic moment,
2.0×10^{25} dyne cm, which agrees closely with the predicted value
from the fault length, fault depth, and dislocation measured
at the epicentral area.

The agreement between theoretical and observed spectra
was excellent for wave paths which lie in the loop direction of
the radiation and consist of laterally uniform crustal structure.
The result confirmed the rupture velocity of 2.2 km/sec obtained
from a near-field measurement. The strike direction determined
from Love and Rayleigh waves better fits the strike of fracture
zones than that obtained from the first motions.

Complex spectra were observed for paths crossing boundaries
of oceans and continents. Some indication of coupling between
Love and Rayleigh waves was noticed for these paths.

Q values are revised by a least squares method applied to the data from all the stations. The ratio of observed spectra to theoretical was plotted against the epicentral distance, and the slope and zero-crossing value are used for revising Q values and seismic moment respectively. The revised value of moment is 1×10^{25} dyne cm. The revised Q values are listed below.

T period		Q continent		Q ocean	
	(sec)	$\dot{R}$	L	R	L
50		>195	∞	>115	>200
25		>400	∞	>210	>545

Reference:

Tsai, Y.B., and K. Aki, Radiation and dissipation of Love and Rayleigh waves from the Parkfield Earthquake of June 28, 1966, (in preparation).
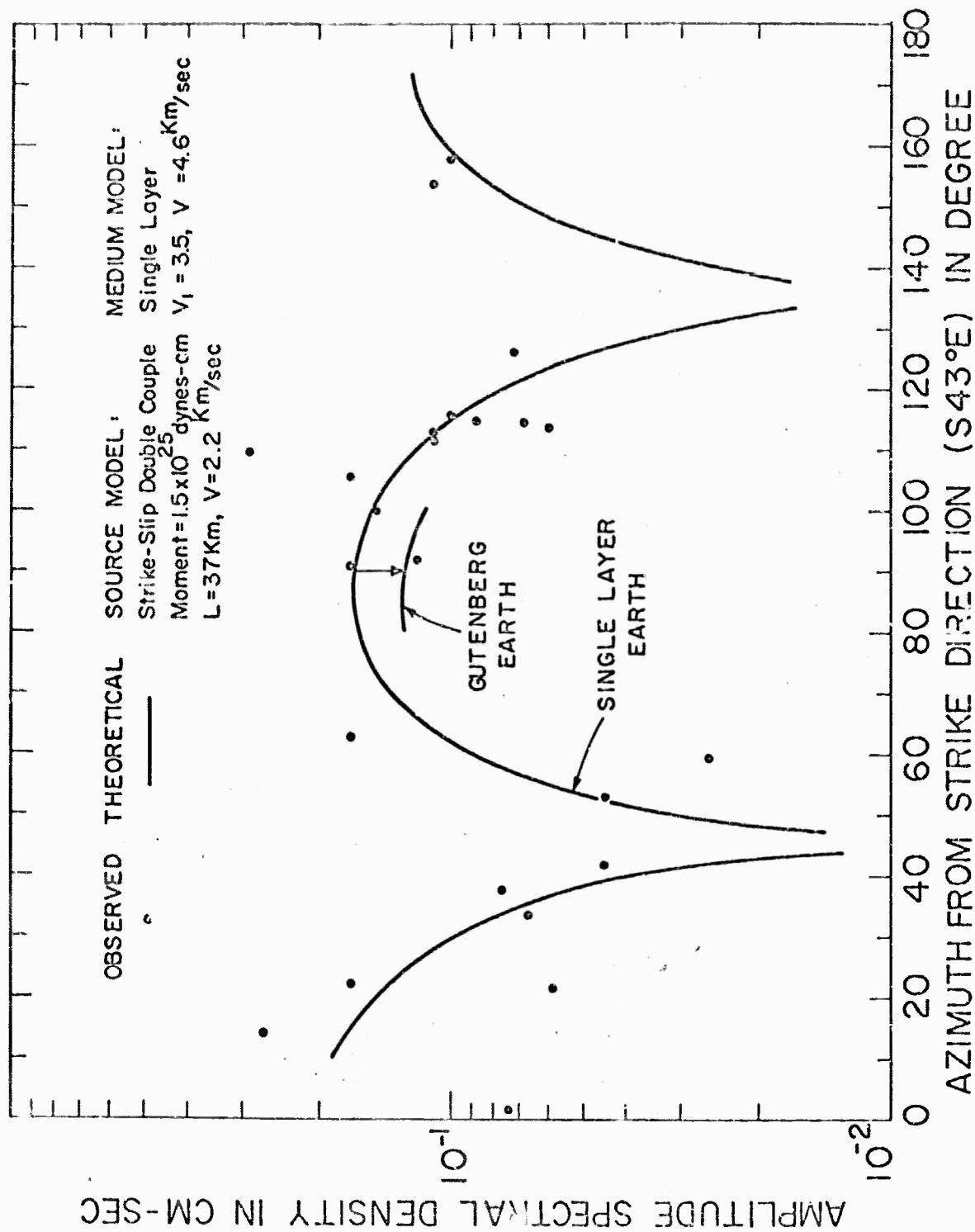
FIG.12 LOVE WAVES WITH PERIOD 50 SEC REDUCED TO 4000 KM

The figure plot contains the following labels:

OBSERVED   THEORETICAL

SOURCE MODEL:
Strike-Slip Double Couple
Moment=1.5x10²⁵ dynes-cm
L=37Km, V=2.2 Km/sec

MEDIUM MODEL:
Single Layer
$V_1 = 3.5$, $V = 4.6$ Km/sec

GUTENBERG EARTH

SINGLE LAYER EARTH

AMPLITUDE SPECTRAL DENSITY IN CM-SEC

AZIMUTH FROM STRIKE DIRECTION (S43°E) IN DEGREE
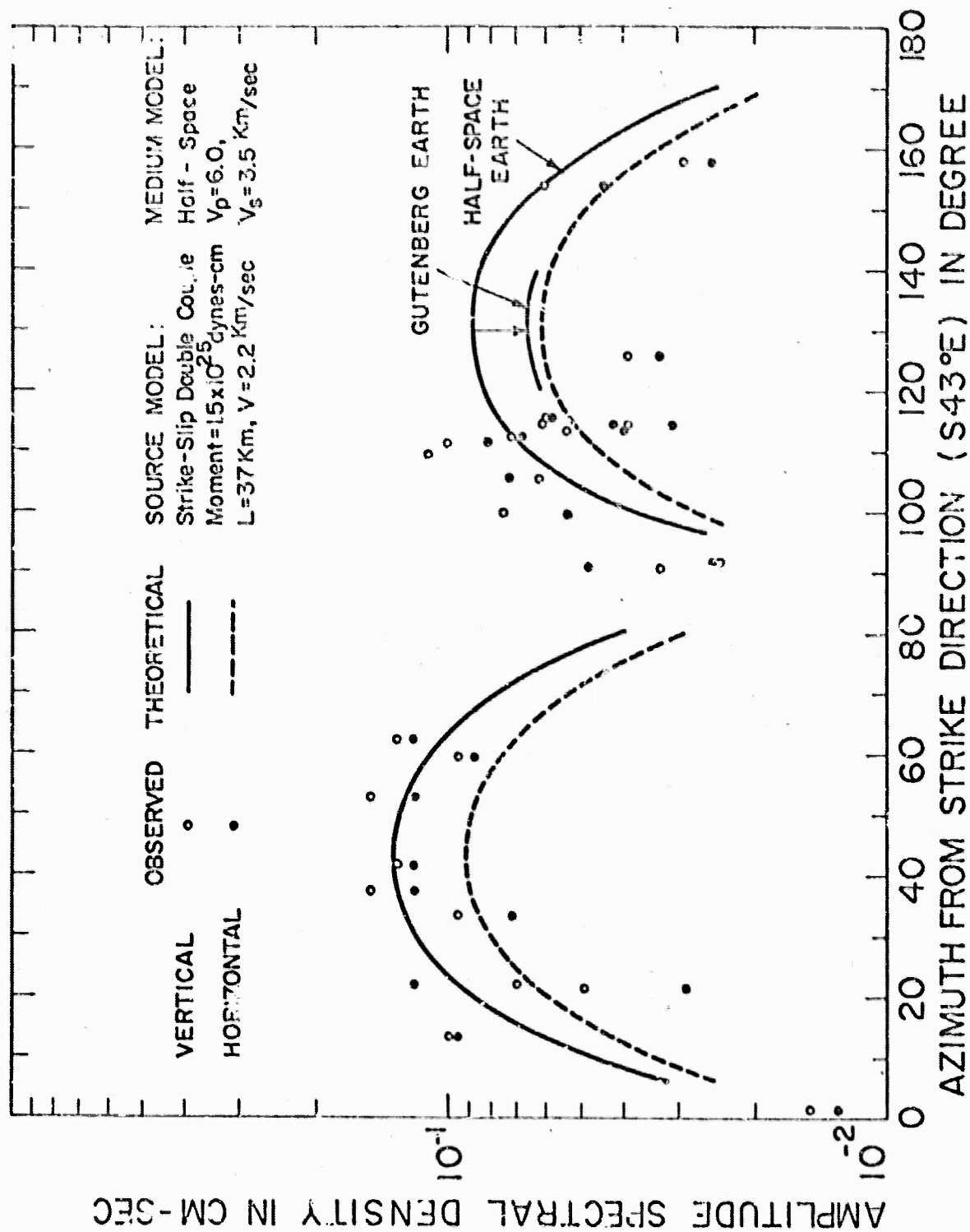
FIG. 1

FIG. 13. RAYLEIGH WAVES WITH PERIOD 50 SEC REDUCED TO 4000 KM

FIG. 5

V.   OTHER DEVELOPMENTS

V.1.   LASA Tape Library

A library of LASA digital tapes containing seismic signals
from earthquakes and explosions is being set up at the Department
of Geology and Geophysics, for facilitating the M.I.T. seismologists'
quick access to the LASA data. It is intended to collect large
seismic signals with high S/N, coming from events covering the
entire earth uniformly.

The library will include the following items for each event,

(1)   high mode or low mode LASA tape

(2)   Sanborn plot of major phases

(3)   listing of relevant data for the event, such as
      epicenter location, origin time, apparent velocity and
      azimuth at LASA, magnitude, amplitude, etc.

In addition, computation of the Fourier transforms of waves
from selected events are made semi-routinely. The result includes
plotting of amplitude spectrum and phase spectrum as a function
of distance across LASA, and also the averaged spectrum for
frequency range from 0.3 to 1.5 cps.

V.2. A Coherent Stationary Seismic Source

Several orders of magnitude increase in accuracy of seismic velocity measurement are required for detecting its change with time. For example, the stress change associated with the earth tide would be detected through the velocity change, if the accuracy is of the order of 10^{-6}. The tectonic stress may be detected with the accuracy of 10^{-4}. The minimum error expected for the conventional method using explosions is of the same order. We need a new technique with greater accuracy for such purposes.

It should be possible to increase the accuracy, by increasing the time spent on measuring the velocity, if the seismic source is precisely controlled with respect to its long-term stability.

A prototype seismic wave generator has been designed and built, using the 1/4 wave length oscillation of water column, as is shown in Figure 1. It has successfully generated seismic waves with desired amplitudes. A detailed study of its function is being made in order to get basic data needed for designing a generator useful for measuring the tectonic stress change in a seismically active area.

Reference:

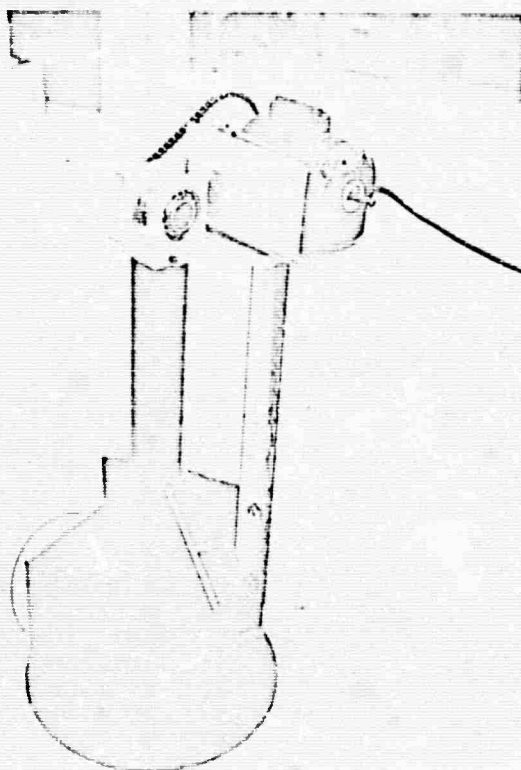T. DeFazio, A coherent seismic force source (in preparation).

FIG. 1

DOCUMENT CONTROL DATA - R&D

(Security classification of title, body of abstract and indexing annotation must be entered when the overall report is classified)

1. ORIGINATING ACTIVITY *(Corporate author)*	2a. REPORT SECURITY CLASSIFICATION
Massachusetts Institute of Technology Department of Geology and Geophysics Cambridge, Massachusetts 02139	Unclassified
	2b. GROUP

3. REPORT TITLE

Research in Seismology

4. DESCRIPTIVE NOTES *(Type of report and inclusive dates)*

Scientific: Annual (1 November 1966 - 31 October 1967)

5. AUTHOR(S) *(Last name, first name, initial)*

Press, Frank and Toksöz, M. Nafi

6. REPORT DATE	7a. TOTAL NO. OF PAGES	7b. NO. OF REFS
12 February 1968	104	39

8a. CONTRACT OR GRANT NO.	9a. ORIGINATOR'S REPORT NUMBER(S)
AF 49(638)-1632	M.I.T. Dept. of Geology and Geophysics
b. PROJECT NO. 8652	No: S(Seismology) -2
c.	9b. OTHER REPORT NO(S) *(Any other numbers that may be assigned this report)*
d.	(AFOSR -67-)

10. AVAILABILITY/LIMITATION NOTICES

Distribution of this document is unlimited

11. SUPPLEMENTARY NOTES	12. SPONSORING MILITARY ACTIVITY
	Air Force Office of Scientific Research. (SRPG) 1400 Wilson Blvd. Arlington, Virginia 22209

13. ABSTRACT

The seismic research activities carried under the contract AF 49(638)-1632 are grouped in four categories.

In the first, the utilization of LASA data for various seismological studies is discussed. P-wave velocity-depth distribution in the mantle is obtained along two profiles. Frequency-wavenumber structure of microseisms are investigated using both the long and short period data from LASA and it is found that at periods shorter than 5 seconds predominant noise peaks correspond to higher mode Rayleigh waves and P-wave noise.

The structure and inhomogeneities of the upper mantle are studied using seismic and other geophysical data. In Japan the surface wave dispersion data are best fitted by a model containing thin soft layers in the upper mantle. Seismic, heat flow, geopotential, surface topography and crustal data are correlated using coefficients of spherical harmonics up to the third order. It is found that some lateral density variations may exist in the upper and lower mantle.

The near source and far-field seismic data from the Parkfield earthquake of 1966 are analyzed for source mechanism and attenuation studies. The stress drop associated with this earthquake is estimated to be about twenty bars. Some peaks and regional differences are found in attenuation curves for the Rayleigh and Love waves.

DD FORM 1473
1 JAN 64

14. KEY WORDS	LINK A		LINK B		LINK C	
	ROLE	WT	ROLE	WT	ROLE	WT
Seismology						
Seismic Velocities						
Earth's mantle						
Source Mechanisms						
Microseisms						
Ellipticity						
Attenuation						

INSTRUCTIONS

1. ORIGINATING ACTIVITY: Enter the name and address of the contractor, subcontractor, grantee, Department of Defense activity or other organization (*corporate author*) issuing the report.

2a. REPORT SECURITY CLASSIFICATION: Enter the overall security classification of the report. Indicate whether "Restricted Data" is included. Marking is to be in accordance with appropriate security regulations.

2b. GROUP: Automatic downgrading is specified in DoD Directive 5200.10 and Armed Forces Industrial Manual. Enter the group number. Also, when applicable, show that optional markings have been used for Group 3 and Group 4 as authorized.

3. REPORT TITLE: Enter the complete report title in all capital letters. Titles in all cases should be unclassified. If a meaningful title cannot be selected without classification, show title classification in all capitals in parenthesis immediately following the title.

4. DESCRIPTIVE NOTES: If appropriate, enter the type of report, e.g., interim, progress, summary, annual, or final. Give the inclusive dates when a specific reporting period is covered.

5. AUTHOR(S): Enter the name(s) of author(s) as shown on or in the report. Enter last name, first name, middle initial. If military, show rank and branch of service. The name of the principal author is an absolute minimum requirement.

6. REPORT DATE: Enter the date of the report as day, month, year, or month, year. If more than one date appears on the report, use date of publication.

7a. TOTAL NUMBER OF PAGES: The total page count should follow normal pagination procedures, i.e., enter the number of pages containing information.

7b. NUMBER OF REFERENCES: Enter the total number of references cited in the report.

8a. CONTRACT OR GRANT NUMBER: If appropriate, enter the applicable number of the contract or grant under which the report was written.

8b, 8c, & 8d. PROJECT NUMBER: Enter the appropriate military department identification, such as project number, subproject number, system numbers, task number, etc.

9a. ORIGINATOR'S REPORT NUMBER(S): Enter the official report number by which the document will be identified and controlled by the originating activity. This number must be unique to this report.

9b. OTHER REPORT NUMBER(S): If the report has been assigned any other report numbers (*either by the originator or by the sponsor*), also enter this number(s).

10. AVAILABILITY/LIMITATION NOTICES: Enter any limitations on further dissemination of the report, other than those imposed by security classification, using standard statements such as:

(1) "Qualified requesters may obtain copies of this report from DDC."

(2) "Foreign announcement and dissemination of this report by DDC is not authorized."

(3) "U. S. Government agencies may obtain copies of this report directly from DDC. Other qualified DDC users shall request through
_____."

(4) "U. S. military agencies may obtain copies of this report directly from DDC. Other qualified users shall request through
_____."

(5) "All distribution of this report is controlled. Qualified DDC users shall request through
_____."

If the report has been furnished to the Office of Technical Services, Department of Commerce, for sale to the public, indicate this fact and enter the price, if known.

11. SUPPLEMENTARY NOTES: Use for additional explanatory notes.

12. SPONSORING MILITARY ACTIVITY: Enter the name of the departmental project office or laboratory sponsoring (*paying for*) the research and development. Include address.

13. ABSTRACT: Enter an abstract giving a brief and factual summary of the document indicative of the report, even though it may also appear elsewhere in the body of the technical report. If additional space is required, a continuation sheet shall be attached.

It is highly desirable that the abstract of classified reports be unclassified. Each paragraph of the abstract shall end with an indication of the military security classification of the information in the paragraph, represented as (TS), (S), (C), or (U).

There is no limitation on the length of the abstract. However, the suggested length is from 150 to 225 words.

14. KEY WORDS: Key words are technically meaningful terms or short phrases that characterize a report and may be used as index entries for cataloging the report. Key words must be selected so that no security classification is required. Identifiers, such as equipment model designation, trade name, military project code name, geographic location, may be used as key words but will be followed by an indication of technical context. The assignment of links, rules, and weights is optional.